UC Berkeley

Title

Bayesian-Optimized Riblet Surface Design for Turbulent Drag Reduction via Design-by-Morphing with Large Eddy Simulation

Permalink

Authors

Lee, Sangjoon

Sheikh, Haris Moazam

Lim, Dahyun Daniel

et al.

Publication Date

2024-01-09

DOI

10.1115/1.4064413

Copyright Information

Peer reviewed

Sangjoon Lee[1]

Department of Mechanical Engineering,
University of California, Berkeley,
Berkeley, CA 94720, USA
email: sangjoonlee@berkely.edu

Haris Moazam Sheikh

Department of Mechanical Engineering,
University of California, Berkeley,
Berkeley, CA 94720, USA
email: harissheikh@berkeley.edu

Dahyun D. Lim

Department of Mechanical Engineering,
University of California, Berkeley,
Berkeley, CA 94720, USA
email: limdan7@berkeley.edu

Grace X. Gu

Department of Mechanical Engineering,
University of California, Berkeley,
Berkeley, CA 94720, USA
email: ggu@berkeley.edu

Philip S. Marcus

Department of Mechanical Engineering,
University of California, Berkeley,
Berkeley, CA 94720 USA
email: pmarcus@me.berkeley.edu

Bayesian-Optimized Riblet Surface Design for Turbulent Drag Reduction via Design-by-Morphing with Large Eddy Simulation

A computational approach is presented for optimizing new riblet surface designs in turbulent channel flow for drag reduction, utilizing Design-by-Morphing (DbM), Large Eddy Simulation (LES), and Bayesian Optimization (BO). The design space is generated using DbM to include a variety of novel riblet surface designs, which are then evaluated using LES to determine their drag-reducing capabilities. The riblet surface geometry and configuration are optimized for maximum drag reduction using the mixed-variable Bayesian optimization (MixMOBO) algorithm. A total of 125 optimization epochs are carried out, resulting in the identification of 3 optimal riblet surface designs that are comparable to or better than the reference drag reduction rate of 8%. The Bayesian-optimized designs commonly suggest riblet sizes of around 15 wall units, relatively large spacing compared to conventional designs, and spiky tips with notches for the riblets. Our overall optimization process is conducted within a reasonable physical time frame with up to 12-core parallel computing and can be practical for fluid engineering optimization problems that require high-fidelity computational design before materialization.

Keywords: Design-by-Morphing (DbM), Large Eddy Simulation, Bayesian Optimization, Drag Reduction, Riblet Surface, Turbulent Channel Flow

1 Introduction

Fluid drag, a force that acts against the movement of an object surrounded by fluid, is an inevitable challenge faced by objects moving through air or water. To combat this energy-consuming problem, nature has evolved various methods to reduce fluid drag [1, 2]. Examples include shark skin's micro-surface [3–5], penguins' microbubble-covered feathers, and hydrodynamic body shape to reduce either friction or pressure drag [6, 7]. These biologically inspired strategies have garnered significant interest in the scientific community due to their potential applications in industries such as transportation and pipelines, where increased energy efficiency is crucial. One area of active research involves replicating the micro-surface structure of shark skin, often simplified in the form of riblets [8] (see Fig. 1), and incorporating it as a surface modification in applications such as aircraft, automobiles, swimsuits, or ship hulls [9]. Unlike a streamlined body, which requires modifying the entire structure, riblets may simply be added to an existing surface in the form of a film [10, 11].

To overcome the limitations of riblet designs imposed by fabrication restrictions, researchers have turned to additive manufacturing to create more complex riblet structures for drag reduction [12, 13]. This has enabled the creation of three-dimensional riblet structures, such as those mimicking the trident shape of shark denticles, through multi-material 3D printing [13]. Additionally, additive manufacturing has facilitated the fabrication of closed channels (pipes) with internal surfaces featuring micrometer-sized denticles that reduce drag compared to smooth channels [14]. Despite the expanded design possibilities offered by additive manufacturing, few riblet designs have emerged that outperform conventional ones, such as triangular, scalloped, or blade riblets. This is because the
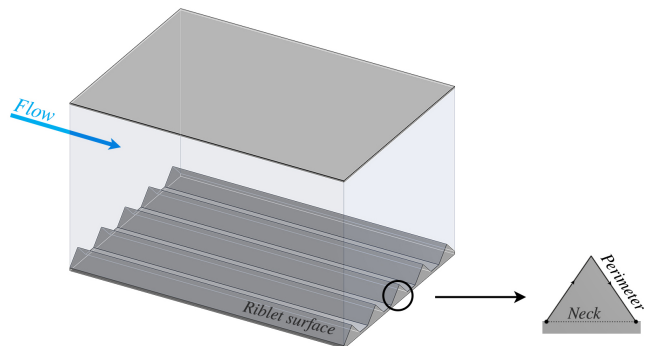
Fig. 1 Configuration of flow over a riblet surface considered in this paper. All riblets are aligned in parallel with the streamwise direction.

removal of manufacturing constraints also means an infinite number of riblet configurations need to be designed and tested. As such, further optimization of riblet structures for drag reduction remains a critical area of research in the broader field of design.

In this study, we employ a combination of Design-by-Morphing (DbM) and Bayesian optimization (BO) to identify and optimize new riblet configurations for drag reduction (See Fig. 2). Our approach involves generating novel riblet shapes by morphing existing ones from the literature and evaluating their drag-reducing capabilities using Large Eddy Simulation (LES) and the Immersed-Boundary (IB) method. The mixed-variable BO algorithm developed by Sheikh & Marcus [15] is then utilized to optimize riblet geometry for maximum drag reduction, resulting in three optimal riblet structures with drag reduction of 8.65%, 8.11%, and 7.84%,
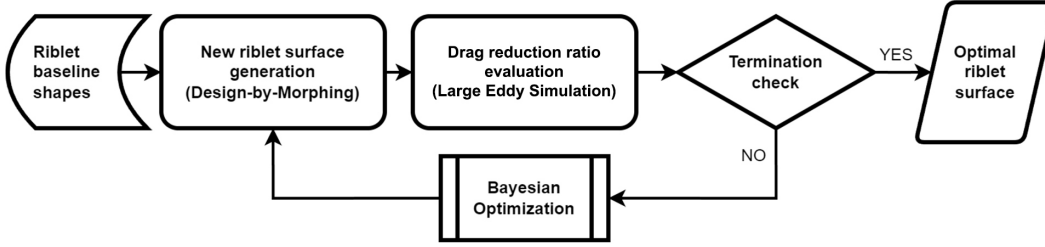
Fig. 2   Computation flowchart for riblet surface design, evaluation and optimization.

respectively. Our findings provide insight into the unique drag-reducing mechanism of these optimized riblet structures, which is thought to be due to the circulation zones created by the spiky tips of the riblets. By combining DbM, LES, and BO, we aim to extend the range of applicability of the riblet structures to a broader range of fluidic conditions by optimizing the riblet configuration.

2   Riblet Surface Design

To systematically explore different riblet shapes, we utilize Design-by-Morphing (DbM). This technique, introduced by Oh *et al.* [16], investigates the aerodynamically optimal shape of a high-speed train for drag reduction. The DbM technique initiates by linearly morphing homeomorphic or, equivalently, topologically equivalent "baseline" shapes to generate continuously varying shapes [17]. The homeomorphic condition establishes a one-to-one correspondence between baseline shapes, which can be performed in either function space [16] or geometric space [17, 18]. Here, we consider morphing in geometric space by representing the boundary of a baseline riblet shape as a set of discrete points that are ordered consistently. If N baseline shapes are reasonably chosen, any new shape created by DbM is expressed as an ordered set of N real values, where the ith value serves as a morphing "weight" for the ith baseline shape. Consequently, using DbM, we construct a continuous mapping of a design space for exploration to a subspace of $\mathbb{R}^N$, which is suitable for further optimization processes such as artificial neural networks [16] or Bayesian optimizations (BOs) [19, 20]. The benchmark study of DbM, demonstrating its excellence in shape construction compared to conventional parameterization methods, can be found in Sheikh *et al.* [17].

2.1   Baseline Shape Selection. According to Sheikh *et al.* [17], diversity in baseline shapes plays a key role in determining how effectively and extensively the design space is established. It is not only important to include conventionally accepted designs as baseline shapes, but it is also worth considering "inferior" performers as part of them. Although each of these baseline shapes may be far from the desired optimum, their combination resulting from DbM provides novelty to the design exploration. This is because negative weights are assigned to these baseline shapes during DbM to allow for *extrapolative* morphing, which is an original feature of the DbM technique that facilitates radical design changes [16].

Following this selection principle, we consider a total of ten riblet shapes ($N = 10$) as the baseline shapes in this study, as depicted in Fig. 3. All of them have been normalized with a unit neck length and height. Due to this, the blade riblet shape appears to be square here. The first eight riblet shapes were suggested in the 1980s [21, 22] and have been widely accepted and studied as riblet surface designs for several decades [23–27]. It is noteworthy that several studies, including Walsh [22] and Bechert *et al.* [23], have reported that riblets with sharp peaks excel in drag reduction. However, for the purpose of exploring our design space extensively, riblets with round or flat peaks are intentionally considered as the baseline shapes.

The last two riblet shapes, which feature a common tapering neck, are original designs proposed in this study. Although they
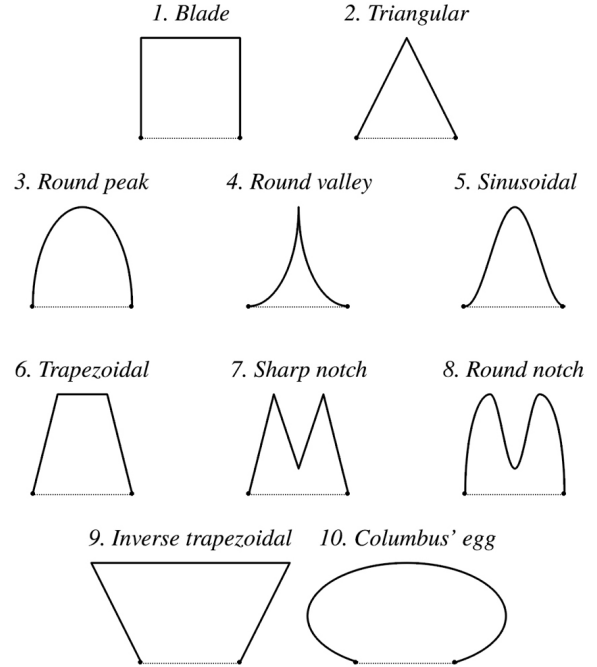

Fig. 3   Baseline riblet shapes for DbM in this study. The first eight are picked from the literature [22], while the last two are originally considered. All riblet baseline shapes depicted here are normalized with a unit neck length and a unit height.

may be revealed as poor performers, they still contribute to the novelty of the design space by explicitly incorporating the tapering-neck feature into our considerations for riblet surface design. This feature may not be achievable through conventional riblet surface production methods, such as rolling processes, as noted in studies such as Klocke *et al.* [28] and Gao *et al.* [29]. However, in the context of additive manufacturing, which is the motivation for the current shape optimization, tapering-neck riblets can be produced, and as such, we believe that they are worth considering.

2.2   Design-by-Morphing. In order to establish one-to-one correspondence between the baseline riblet shapes, we use curve parameterization. In the two-dimensional Cartesian coordinate system (x, y), let's suppose a variable t that parameterizes the wetted perimeter of a riblet shape $\mathcal{R}$ such that

$$\mathcal{R}(t) \equiv \begin{bmatrix} x(t) \\ y(t) \end{bmatrix} \quad 0 \leq t \leq 1, \tag{1}$$

where $\mathcal{R}(t = 0) = (0, 0)$ and $\mathcal{R}(t = 1) = (1, 0)$. That is, the initial and final points correspond to the left and right ends of the riblet neck, respectively. The presence of t is manifest if we interpret t as time and imagine someone *drawing* the curve from left to right in a unit time on condition with respect to the total arc length of

$\mathcal{R}$, denoted L, that

$$L = \int_0^1 \mathcal{R}'(\tau)d\tau. \qquad (2)$$

We keep the drawing speed $\mathcal{R}'(t)$ to be consistently L, and then $\mathcal{R}(t)$ is well-defined. Under this parameterization, all 10 baseline riblet shapes $\mathcal{R}_1, \cdots, \mathcal{R}_{10}$ establish the mutual one-to-one correspondence for all t in $[0, 1]$.

The parameterization above should be discretized for the sake of computation. If we discretize t to t_j for $j = 0, 1, \cdots, p$ such that $0 = t_0 < t_1 < \cdots < t_p = 1$ that are equally spaced (i.e. $t_j = j/p$), we obtain the discretized form of the ith baseline riblet shape $\mathcal{R}_{i,discrete}$ as the following $2 \times (p+1)$ matrix

$$\mathcal{R}_{i,discrete} = \begin{bmatrix} \mathcal{R}_{i,discrete}^0 & \cdots & \mathcal{R}_{i,discrete}^p \end{bmatrix}, \qquad (3)$$

where the $(j+1)$th column $\mathcal{R}_{i,discrete}^j$ is

$$\mathcal{R}_{i,discrete}^j = \begin{bmatrix} x_i(t_j) \\ y_i(t_j) \end{bmatrix}. \qquad (4)$$

As a result, this discrete form is identical to $(p+1)$ points that are equispaced along the wetted perimeter of the riblet shape. In this study, we put $p = 1000$ to numerically represent the baseline riblet shapes. Unless needed, the "discrete" notation, as in Eqs. (3) and (4), is omitted henceforth.

A morphed riblet shape via DbM $\mathcal{M} = \begin{bmatrix} \mathcal{M}^0 & \mathcal{M}^1 & \cdots & \mathcal{M}^p \end{bmatrix}$ from the 10 baseline riblet shapes $\mathcal{R}_1, \cdots, \mathcal{R}_{10}$ is defined as

$$\mathcal{M}^j = \begin{bmatrix} \left(\sum_{i=1}^{10} \omega_i x_i(t_j) - C_1 \right) / C_2 \\ \left| \sum_{i=1}^{10} \omega_i y_i(t_j) \right| / C_3 \end{bmatrix} \quad (j = 0, 1, \cdots, p), \qquad (5)$$

where ω_i is the morphing weight assigned for $\mathcal{R}_i$. C_1, C_2 and C_3 are the renormalization factors defined as follows:

$$C_1 = \min_{j=0, \cdots, p} \left(\sum_{i=1}^{10} \omega_i x_i(t_j) \right), \qquad (6)$$

$$C_2 = \max_{j=0, \cdots, p} \left(\sum_{i=1}^{10} \omega_i x_i(t_j) \right) - C_1, \qquad (7)$$

$$C_3 = \max_{j=0, \cdots, p} \left| \sum_{i=1}^{10} \omega_i y_i(t_j) \right|. \qquad (8)$$

The absolute value of the weighted sum of the y coordinates is taken to avoid negative y because we suppose the riblets to be *additively* manufactured on a flat surface. The renormalization factors make the morphed riblet shape fit into a unit box $[0, 1] \times [0, 1]$ since we later take into consideration their scaling after the morphing (see §2.4).

The supplemental handling of the morphed riblet shape facilitates the effective truncation of the 10-dimensional weight space $\omega = (\omega_1, \cdots, \omega_{10}) \subseteq \mathbb{R}^{10}$. First of all, it is sufficient to examine only the unit hypersphere (i.e. 9-sphere) centered at the origin $\|\omega\|_2 = 1$ because all positive multiples of a weight set $(\omega_1, \cdots, \omega_{10})$ result in the same morphed shape. This reduces the number of independent variables of the design space (i.e. dimensionality) by one. Introducing the 9-dimensional angular coordinates $(\varphi_1, \cdots, \varphi_9)$ for $\varphi_1, \cdots, \varphi_8 \in [0, \pi]$ and $\varphi_9 \in (-\pi, \pi]$
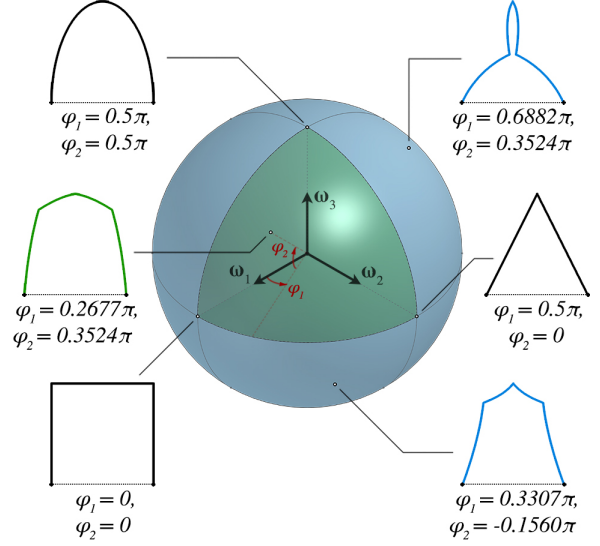
Fig. 4 **Truncated weight space visualized on the hemispherical surface in the 3D subspace $(\omega_1, \omega_2, \omega_3)$, parameterized by φ_1 and φ_2. Interpolative morphing occurs in the green zone, while extrapolative morphing happens in the blue zone.**

[30] may be useful in this case, which are related to the weight variables through
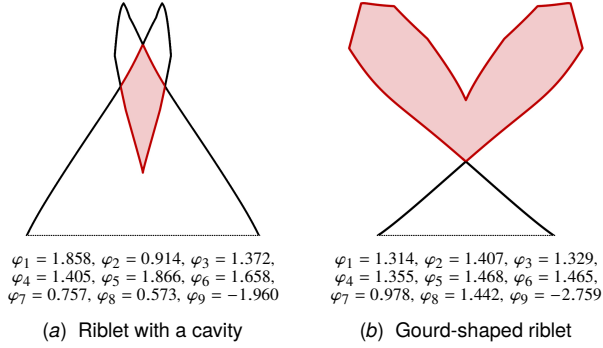
$$\omega_i = \begin{cases} \cos(\varphi_1) & i = 1 \\ \left[\prod_{k=1}^{i-1} \sin(\varphi_k) \right] \cos(\varphi_i) & i = 2, \cdots, 9 \\ \prod_{k=1}^{i-1} \sin(\varphi_k) & i = 10 \end{cases} \qquad (9)$$

Furthermore, it is safe to ignore one half of the hypersphere because a morphed shape from $-\omega$ is no more than a mirrored image of that from ω. We pick the half where $\sum_{i=1}^{10} \omega_i \geq 0$ that encompasses the *interpolative* morphing region where $\omega_i \geq 0$ for all $i = 1, \cdots, 10$. If all weights are non-negative, interpolation morphing occurs with modest transition. Otherwise, if some are negative, extrapolation morphing is performed, allowing radical design change. The visual illustration of the truncated weight space is exhibited in Fig. 4 in its 3D subspace $(\omega_1, \omega_2, \omega_3)$ for simplification (i.e. $\omega_4 = \cdots = \omega_{10} = 0$), where all morphed shapes are mapped on the unit hemispherical surface that can be parameterized by $\varphi_1 \in [0, \pi]$ and $\varphi_2 \in (-\pi, \pi]$.

2.3 Geometrical Feasibility Check. In the truncated weight space $\|\omega\|_2 = 1$ and $\sum_{i=1}^{10} \omega_i \geq 0$, denoted $\mathcal{W}$, not all of the morphed riblet shapes are geometrically feasible because some may result in non-physical features, represented by self-intersections. Examples of self-intersecting riblet shapes are shown in Fig. 5. Although this is not a problem for interpolation (i.e., when all weights are non-negative), it becomes problematic when it comes to extrapolation (i.e., when some weights are negative), which we allow to enable radical design changes. To computationally detect self-intersections of a given shape, we utilize the MakeValid function provided by the GEOS C/C++ library [31], which transforms a single shape to multi-geometries in case of self-intersections by scanning the input vertices (i.e., $(p+1)$ points in $\mathcal{M}$). The function queries a subset of the vertices that can form a simple closed curve (ring) and iterates this process until no more rings can be found with the remaining vertices. If the function outputs two or more rings, then the input is determined to be self-intersecting.

The treatment of self-intersections depends on how much tolerance there is for such invalid geometries. For instance, in the airfoil optimization study with DbM by Sheikh *et al.* [17], self-intersecting shapes were slightly buffered at the self-intersections

$\varphi_1 = 1.858$, $\varphi_2 = 0.914$, $\varphi_3 = 1.372$,
$\varphi_4 = 1.405$, $\varphi_5 = 1.866$, $\varphi_6 = 1.658$,
$\varphi_7 = 0.757$, $\varphi_8 = 0.573$, $\varphi_9 = -1.960$

(a) Riblet with a cavity

$\varphi_1 = 1.314$, $\varphi_2 = 1.407$, $\varphi_3 = 1.329$,
$\varphi_4 = 1.355$, $\varphi_5 = 1.468$, $\varphi_6 = 1.465$,
$\varphi_7 = 0.978$, $\varphi_8 = 1.442$, $\varphi_9 = -2.759$

(b) Gourd-shaped riblet

Fig. 5   Invalid morphed riblet shapes with self-intersections.

Fig. 6   Overall DbM process for designing riblet surface.

and recovered. In this problem, however, we discard these self-intersecting shapes (cf. [18]) because we see no practical benefit in recovering them. In the context of our study, the self-intersections create either a cavity structure in the riblet or a gourd-shaped structure on it, both of which are believed to be neither favorable for drag reduction nor structurally stable.

2.4   Riblet Scaling and Spacing. The DbM technique described so far composes morphed riblet shapes that are confined in a unit box. Thus, it is necessary to scale the width w and height h of the riblet to consider the effects of size and aspect ratio. In addition, the spacing between the riblets s is taken into account, which is a necessary parameter for some riblet surfaces, like the blade riblet surface. Fig. 6 depicts the implementation of the morphed riblet surface design in the channel after scaling and spacing with the three parameters w, h, s. Here, $w > 0$, $h > 0$, and $s \geq 0$.

Walsh & Lindemann [32] reported that the use of wall units for scaling provided consistent results, regardless of the Reynolds number or previous boundary-layer history. Many subsequent studies, including those by Choi *et al.* [33] and García-Mayoral & Jiménez [34], have adopted this scaling rule with success. We also utilize the wall unit scaling, commonly denoted with the + superscript. The wall units are defined as

$$w^+ \equiv \frac{wu_\tau}{\nu}, \quad h^+ \equiv \frac{hu_\tau}{\nu}, \quad s^+ \equiv \frac{su_\tau}{\nu}, \tag{10}$$

where ν is the fluid kinematic viscosity and $u_\tau \equiv \sqrt{\overline{\tau_w}/\rho}$ is the wall-shear velocity. ρ denotes the fluid density and $\overline{\tau}_w$ indicates the mean wall shear stress. For a channel flow, the channel half-width ς in the wall unit scaling is called the friction Reynolds number Re_τ, that is,

$$Re_\tau = \frac{\varsigma u_\tau}{\nu}. \tag{11}$$

This dimensionless parameter is going to be essential in determining the bulk flow characteristics in later numerical simulations (see §3.2). According to literature [22, 23, 34, 35], the range of w^+ or h^+ in which the optimum is expected to exist is around 15, and therefore, it seems sufficient to set their upper limit to 30. For s^+, to avoid too sparse riblets or, equivalently, to prevent them from making little difference from a flat surface, we limit it up to 50.

The parametric space of the scaling and spacing parameters $s = (w^+, h^+, s^+) \subset \mathbb{R}^3$, denoted $\mathcal{S}$, comprises another essential design space in tandem with the feasible, truncated weight space $\mathcal{D}$. Consequently, the resulting design space in which we investigate for the optimization should be $\mathcal{D} \times \mathcal{S}$. The space is spanned by 9 independent variables for morphing, φ_1, φ_1, $\cdots$, φ_9, and 3 independent variables for scaling and spacing, w^+, h^+, s^+, in total 12 real-valued variables.
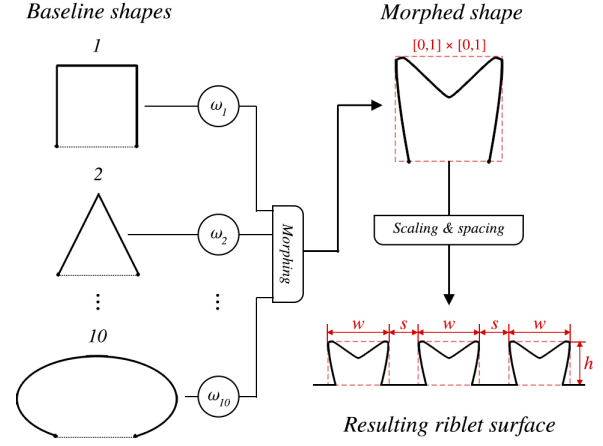
3   Flow Simulation

For the performance evaluation within the design space $\mathcal{D} \times \mathcal{S}$, we use a full, non-linear, incompressible Navier-Stokes equation solver with subgrid-scale modeling proposed by Lee & Hwang [36]. Although the solver includes a heat transfer analysis module, which we may consider for later optimization, in this present study, we only utilize and focus on its momentum solution (i.e., drag force). We note that the momentum solver has already been applied to the ribbed passage simulation for the internal cooling flow of gas turbine blades and was validated successfully with comparisons to experimental results in the study by Baek *et al.* [37].

A number of numerical studies for the drag reduction of riblet surfaces have used a Reynolds-Averaged Navier-Stokes (RANS) solver to simulate turbulent flows [25–27]. It offers a relatively fast and decent understanding of flow dynamics over the riblets. However, the RANS-based solver typically requires some key information on turbulence prior to computation, such as turbulent kinetic energy. The turbulence characteristics of the flow can be dependent on the turbulence input, which is believed to be less appropriate for the current problem where drag reduction is highly likely to originate from turbulence-producing structures interacting with the riblet surface [33, 38]. On the other hand, there is a Direct Numerical Simulation (DNS) solver for the Navier-Stokes equations [33]. It provides a great match with experimental results (e.g., Walsh [21]) yet generally requires too exhaustive computing resources to resolve the natural dissipation length scale, i.e., the Kolmogorov length scale [39]. In the optimization aspect, the DNS solver is too costly to be run repeatedly hundreds of times.

Our solver, belonging to the Large Eddy Simulation (LES) solvers, is based on the full Navier-Stokes equations, similar to DNS. However, it allows for a larger grid size than DNS because the subgrid-scale motion is modeled. As the subgrid-scale modeling works using the relatively large eddy motion from turbulence resolved at each time step, the computation can proceed without the pre-manipulation of turbulence information. Moreover, the solver takes advantage of the Immersed-Boundary (IB) method [40] to form the riblet surface in the post-meshing stage. Therefore, mesh-independent results can be generated if the same grid input is applied, which is appropriate for comparison purposes.

3.1   Governing Equations. The essential form of the governing equations can be expressed as in the following:

$$\frac{\partial u_i}{\partial x_i} = 0, \tag{12}$$

$$\frac{\partial u_i}{\partial t} = -\frac{\partial u_i u_j}{\partial x_j} - P\delta_{1i} - \frac{\partial \bar{p}}{\partial x_i} + \frac{1}{Re_\tau}\frac{\partial^2 u_i}{\partial x_j x_j} - \frac{\partial \tau_{ij}}{\partial x_j}, \tag{13}$$

where x_i and u_i are the three-dimensional Cartesian coordinates and velocity components, respectively, t is the time, P is the constant pressure gradient in the x_1 direction (δ_{jk} indicates the Kronecker delta), $\tilde{p}$ is the residual pressure, and τ_{ij} is the subgrid-scale stress. All of the variables presented above are non-dimensionalized by the channel half-width ς (given no riblets), the fluid density ρ, and the wall-shear velocity u_τ, making Re_τ appear in the momentum equation. We use $Re_\tau = 180$ for all simulations to take advantage of a plenty of the DNS references at this Reynolds number condition [33, 41–44]. As for the flow direction, we consider x_1 as the streamwise direction, x_2 as the wall-normal direction, and x_3 as the spanwise direction.

We decompose the pressure field p into P and $\tilde{p}$ as $p = Px_1 + \tilde{p}$, where P is kept constant to serve as the driving force in the streamwise direction during the simulation. Given that the flow is fully developed and there is no residual pressure in a spatially averaged manner, $P = -1$. This is because in the dimensional form, the constant pressure gradient equals to $-\rho u_\tau^2/\varsigma$.

The subgrid-scale stress term τ_{ij} is calculated using the subgrid-scale eddy viscosity model proposed by Vreman [45]. As with the classical, renowned model by Smagorinsky [46], the model employs the subgrid-scale stress tensor formula

$$\tau_{ij} - \frac{1}{3}\tau_{kk}\delta_{ij} = -2\nu_T S_{ij} \tag{14}$$

where ν_T is the subgrid-scale eddy viscosity and S_{ij} is the rate-of-strain tensor. The model evaluates ν_T in the following way [44, 45]:

$$\nu_T = c\sqrt{\frac{B_\beta}{\alpha_{ij}\alpha_{ij}}}, \tag{15}$$

$$\alpha_{ij} = \frac{\partial u_j}{\partial x_i}, \tag{16}$$

$$B_\beta = \beta_{11}\beta_{12} - \beta_{12}^2 + \beta_{11}\beta_{33} - \beta_{13}^2 + \beta_{22}\beta_{33} - \beta_{23}^2, \tag{17}$$

$$\beta_{ij} = \Delta_m^2 \alpha_{mi}\alpha_{mj}, \tag{18}$$

where c is the model coefficient and Δ_m indicates the local grid interval dimensions. If α_{ij} is zero, then ν_T is forced to be zero. Unlike the model of Smagorinsky [46], the present subgrid-scale model inherently constructs the subgrid-scale eddy viscosity that correctly vanishes in the region where the dissipation is theoretically believed to be zero [44]. In this work, we use $c = 0.07$, following the previous results from Vreman [45] and our *a priori* tests of turbulent channel flows at $Re_\tau = 180$. Although some dynamic models that internally determine c in terms of time [36, 44] can be considered to improve the model's autonomy, we decided to maintain the constant model coefficient to avoid its recalculation at every time step, as it significantly increases the total computation time and aggravates the time-efficiency of the optimization.

3.2 Computational Domain Setup and Validation.

Fig. 7 presents our computational domain. The no-slip condition is imposed on the wall regions, and periodic boundary conditions are applied to both x_1 and x_3 directions. The wall-normal computational domain length X_2 is expected to be 2, considering the channel half-width ς as a reference, without the riblet surface. Referring to the DNS study by Choi *et al.* [33], we set the streamwise computational period X_1 to π and the spanwise computational period X_3 to around 1. However, with the consideration of the riblet surface later, X_3 might slightly vary around 1 to maintain geometric periodicity in the spanwise direction. Additionally, X_2 might end up being slightly larger than 2 to offset the channel's cross-sectional area loss caused by the riblets. As a result, the cross-sectional area remains consistently $2X_3$.

Table 1 Comparison of computed mean streamwise velocity gradients at the wall with no riblets.

| Database	Type	$\Delta_{2,\max}^+$	Re_τ	$(\partial\overline{u}_1/\partial x_2)\vert_w$	% Error
[41]	DNS	4.4	180	179.93*	-0.04%
[42]	DNS	5.9	180	180.06*	0.03%
[47]	LES	20	180	177.84	-1.20%
Present	LES	14	180	181.21	0.67%

* values calculated from the computed skin friction coefficient C_f ($\equiv 2u_\tau^2/U_b^2$) as $\sqrt{C_f/2} \cdot U_b\,\varsigma/\nu$ where U_b is the computed mean bulk velocity.

The grid dependency of the current method for turbulent channel flows was studied by Lee & Hwang [36] at a similar Reynolds number of $Re_\tau = 150$. Our *a priori* tests at $Re_\tau = 180$ without riblets also reveal a convergence trend (with respect to the grid size) of the *computed* mean streamwise velocity gradient at each channel wall ($\partial\overline{u}_1/\partial x_2)\vert_w$ to its *theoretical* value, equal to Re_τ, under the current non-dimensionalization based on ρ, u_τ, and ς. As a result, we use the grid cells of $16 \times 108 \times 320$, the finest one among the tests yielding the mean streamwise velocity gradient within an error of 0.67% (see Table 1).

Uniformly distributed grid lines with a constant spacing $\Delta_1^+ = 35.34$ are used in the streamwise direction, corresponding to the streamwise spacing condition of Choi *et al.* [33]. The uniform mesh size is also used up to the 32$^{\text{nd}}$ wall-normal grid lines, which are located away from each wall, corresponding to $y^+ = 30$, as well as for the entire spanwise grid lines. This ensures that $\Delta_2^+ = 0.9375$ and $\Delta_3^+ \approx 0.5625$ near the walls, which are fine enough to resolve the geometry of the riblet surface implemented as an immersed boundary, as well as near-wall flow features. The remaining wall-normal grid lines are deployed over the channel center with a hyperbolic tangent distribution, with the maximum spacing of 14 wall units at the channel centerline and the minimum spacing of 1 wall unit right above and below the uniform region. It is noted that any length value given in wall units in a dimensionless manner, e.g., ξ^+, should be expressed as ξ^+/Re_τ in the computational domain, as ς serves as the reference scale. The spatial differentiation and time integration are conducted using the finite volume method of Kim *et al.* [40], which is based on a second-order central difference method for space and a semi-implicit fractional-step method for time [36]. The time step interval is controlled by the Courant-Friedrichs-Lewy (CFL) condition, where the maximum CFL number is empirically chosen to be three.

In Table 1, our computed result of $(\partial\overline{u}_1/\partial x_2)\vert_w$ for the turbulent channel flow with no riblets at $Re_\tau = 180$ is compared to previous numerical studies [41, 42, 47]. Our result is the average of $(\partial\overline{u}_1/\partial x_2)\vert_w$ obtained from three independent simulation runs with small random perturbation seeds of $O(10^{-5})$ applied to the still fluid at the beginning, which helps to reach different yet statistically identical turbulent solutions. In each run, the mean is taken both spatially and temporally over a time interval of 162.5 (where a unit time is equivalent to ς/u_τ in dimensional form) after the flow becomes turbulent and statistically steady. This time interval for averaging is comparable to or longer than in previous numerical studies [33, 43] and confirms a zero-percent difference of $(\partial\overline{u}_1/\partial x_2)\vert_w$ between the lower and upper walls within a standard deviation of 1 percentage point.

Finally, the riblet surface of interest, selected from the design space $\mathcal{D}\times\mathcal{S}$, is implemented using the immersed-boundary method introduced by Kim *et al.* [40]. After the grid points are classified into inner-body and outer-body points across the riblet surface, virtual mass source (or sink) term m and momentum forcing term f_i are added to the right-hand sides of Eqs. (12) and (13), respectively, to construct the immersed boundary within which the flow velocity is zeroed out, i.e. $u_i = 0$, while maintaining the continuity

(a) $x_2 x_3$-plane

(b) $x_1 x_2$-plane
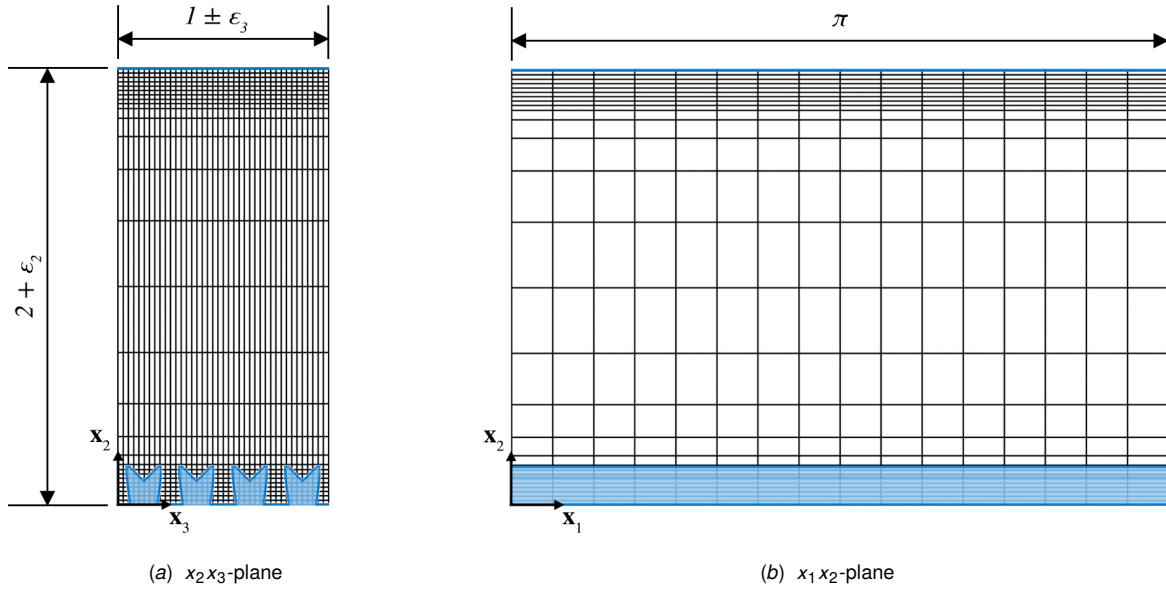
Fig. 7 Computational domain with Cartesian grid layout (the grid rendered here is coarser than what is actually used). ε_2 and ε_3 are to keep the same channel cross-sectional area and to maintain the geometric periodicity in the spanwise (x_3) direction, respectively. For a simulation with no riblets, $\varepsilon_2 = \varepsilon_3 = 0$.

in the computational domain. Also, the no-slip boundary condition is satisfied at the boundary so that we ultimately acquire the correct flow solutions over the riblet surface of interest. For further information on how m and f_i are determined to create the immersed boundary from a given surface or body while preserving second-order spatial accuracy, one may refer to Kim *et al.* [40]. Fig. 8 illustrates the use of the immersed-boundary method for a given riblet surface. To establish the no-slip boundary condition, f_i alters the interface velocity of its action point, e.g. U_{3c} in the dashed box, and makes the linear interpolation of the adjacent velocity components at the boundary point nearest the action point, e.g. a red dot in the dashed box, zero. m then corrects the continuity.

3.3 Drag Reduction Measurement. One of the benefits of utilizing the immersed-boundary method is that the momentum forcing term, f_i, furnishes information about the force acting on the body. In general, the intricate geometry of the riblet surface makes it challenging to calculate the drag force D directly from the surface integral of the wall shear stress, particularly on parts of the surface that are curved or unaligned with the grid lines. On the other hand, employing the immersed-boundary method, the equivalent force can be expressed as

$$D = \int_{\mathcal{F}} \left(\frac{1}{Re_\tau} \left. \frac{\partial u_1}{\partial x_2} \right|_w \right) dS + \int_{\mathcal{V}} P dV$$

$$- \int_{\mathcal{V}} f_1 dV + \int_{\mathcal{V}} \left(\frac{\partial u_1}{\partial t} + \frac{\partial u_1 u_j}{\partial x_j} \right) dV,$$

(19)

where $\mathcal{F}$ is the wetted flat surface remaining on the wall due to the riblet spacing and $\mathcal{V}$ corresponds to the riblet volumes. All the integrals can be numerically calculated without complications. In Eq. (19), the last term in the right-hand side is the convective term derived by Lee *et al.* [48]. Although this term appears redundant because $u_1 = 0$ throughout $\mathcal{V}$, it is retained because it can serve as a correction term numerically computing Eq. (19), and accordingly, the volume integral of f_i in the third term on the right-hand side only becomes approximately correct.

Our interest is in the mean reduction in drag of the riblet surface compared to that of the flat surface. At every time step of computation, we obtain the numerically computed drag force acting on
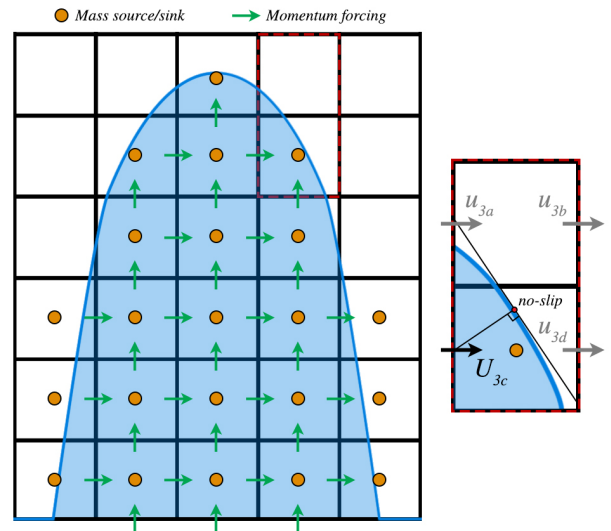

Fig. 8 Riblet surface generation in an immersed boundary form. Mass source/sink m and momentum forcing f_i terms are added to zero out the flow velocity in the riblet (solid) region. See Kim *et al.* [40] for further details.

the lower wall of the riblet surface D_r and another one acting on the upper wall of the flat surface D_f using Eq. (19). We then calculate the instantaneous percentage drag reduction ratio, which is given by $(1 - D_r/D_f) \times 100\%$, varying over time. To extract the mean statistic, we time-average D_r and D_f, and finally obtain the mean percentage drag reduction ratio, DR, as

$$DR = \left(1 - \frac{\frac{1}{T} \int_{t_i}^{t_i+T} D_r(\tau) d\tau}{\frac{1}{T} \int_{t_i}^{t_i+T} D_f(\tau) d\tau} \right) \times 100\%, \qquad (20)$$

where t_i and T are consistently set to 32.5 and 162.5 non-
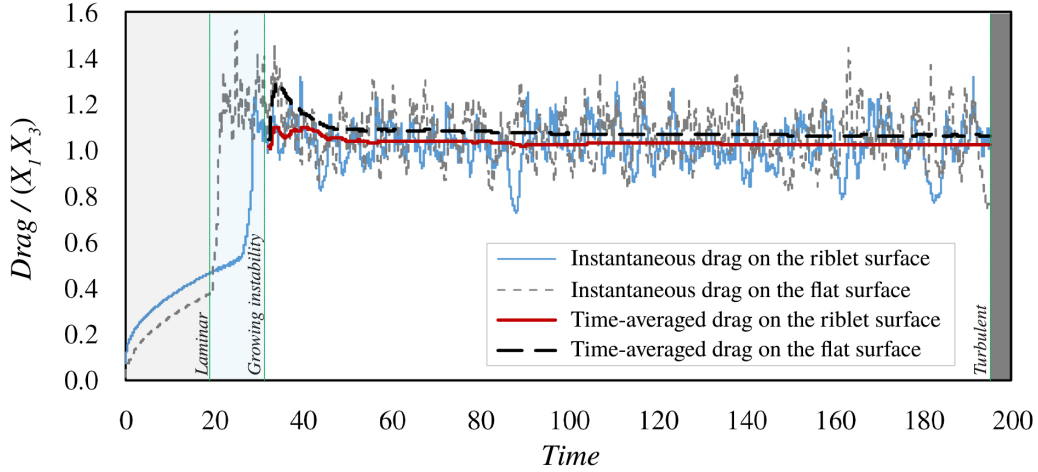
Fig. 9 Time history of the drags on the flat surface and on the riblet surface of the triangular shape of $w^+ = h^+ = 20$ and $s^+ = 0$. Flow instability is invoked at $t \approx 19.5$ and time-averaging is performed during the turbulent stage from $t = 32.5$ to $t = 195$. Note that t and $D/(X_1 X_3)$ are dimensionless using the scaling quantities ς/u_τ and ρu_τ^2, respectively.

dimensional time units, respectively. Fig. 9 exhibits the time history of D_r, D_f, and their mean statistics that start at $t = t_i$ with the triangular riblet surface having $w^+ = 20$, $h^+ = 20$ and $s^+ = 0$. We begin with the initial fluid of no bulk velocity. The time history confirms that $T = 162.5$ is sufficient to generate statistically steady results. Regardless of the riblet surface to be evaluated, it should be ensured that the entire flow becomes turbulent before $t = t_i = 32.5$. To achieve this, the instability is deliberately triggered when the flow forms the laminar velocity profile, driven by P, whose volume flow rate surpasses 90% of the mean volume flow rate found in the previously examined flat channel flow case. The instability is typically invoked around $t = 19.5$ by the superposition of the sinusoidal perturbation velocity profile suggested by De Villiers [49] onto the laminar velocity profile. The perturbation is initially imposed near the upper flat wall and then rapidly develops into turbulence over the entire channel after around 10 non-dimensional time units (cf. Vreman & Kuerten [43]), i.e., at $t = 29.5 < t_i$.

For validation, some results with the triangular riblet surface are compared with the previous experimental and DNS results [21, 33] in Table 2. Like the previous turbulent channel flow simulations with no riblets, DR is evaluated three times from three independent simulation runs for each case, and the average is calculated. The standard deviations are all again within 1 percentage point. All the results, including ours, reveal the drag reduction ratios in the descending order of cases D, C, A, and B in common. Considering the fact that the maximum percentage point difference of the DNS results [33] from the experiments [21] among these cases is 3 percentage points (case B), we believe that our measurements are in reasonable agreement with the experiments. The experimental measurements by Walsh [21] were obtained from the drag measuring system with an error bound of $\pm 1\%$. From error propagation, the error bound for the drag reduction ratio is expected to be larger than ± 1 percentage points. As a result, when it comes to the favorable drag reduction ratios (cases C and D), it turns out that the mean drag reduction rate obtained from our simulations matches the experiments within the error bound, showing a better agreement than the DNS results.

4 Bayesian Optimization

Optimizing expensive black-box functions that involve categorical or mixed variables is an active area of research. For these complex problems, Bayesian optimization (BO) has proven to be highly efficient, using a smaller number of function calls compared to other optimization strategies [50]. Considering the relatively ex-

Table 2 Drag reduction ratios of the triangular riblet surface of different scales.

Case	w^+	h^+	s^+	Present (% point error)	DNS [33] (% point error)	Exp. [21]
A	40	20	0	-3.79% (-0.79%)	-2% (1%)	-3%
B	40	40	0	-8.02% (2.98%)	-12%* (-1%)	-11%
C	20	10	0	3.00% (1.00%)	5% (3%)	2%
D	20	20	0	3.40% (-0.60%)	6%* (2%)	4%

* data obtained from the equilateral triangular riblet surface ($h^+ = \sqrt{3}/2w^+$).

pensive evaluation stage (LES) for each design case, BO is selected as an optimizer to make our optimization framework work in practice.

Many engineering optimization problems have utilized a mixed-variable design space, as seen in architected material design [19, 20, 51–55], hyper-parameter tuning for machine learning algorithms [56–58], drug design [59, 60] and fluid structure design [17, 18, 61]. The current ribbed channel optimization problem may also be considered in a mixed-variable space. Our design space $\mathcal{D} \times \mathcal{S}$ is parameterized by the 9 angular coordinate variables ($\varphi_1, \cdots, \varphi_8, \varphi_9$) and the 3 scaling and spacing variables (w^+, h^+, s^+), as described in §2.4, and the most accurate way to search this space is to treat all 12 variables as entirely continuous. For noisy and multi-modal objective evaluations, such as LES simulations, optimization algorithms can get stuck in local optima and over-explore a limited section of space [18]. In such cases, it is efficient to select a finite set of reasonable (e.g., equally spaced) values for each variable and handle them in a discrete manner. This reduces any redundant search that might take place on a design point too close to previously evaluated points, ensuring distances among potential search points. For example, we formally select

$$\varphi_k \in \left\{ \frac{n}{N_k}\pi \,\middle|\, n = 0,\ 1,\ \cdots,\ N_k \right\} \subset [0, \pi], \qquad (21)$$

for the first 8 angular coordinate variables spanning $\mathcal{D}$ ($k =$

1, $\cdots$, 8) (recall Fig. 4 for their geometric expression), and

$$\xi^+ \in \left\{ \frac{m}{M_\xi} \xi_{max}^+ \;\middle|\; m = (0,\,)1, \cdots, M_\xi \right\} \subset [0, \xi_{max}^+], \quad (22)$$

for the scaling and spacing variables spanning $\mathcal{S}$ ($\xi = w$, h, s), where $m = 0$ must be excluded for the scaling variables to avoid zero width or height (recall Fig. 6 for their geometric expression). However, the selection formalism in Eq. (21) cannot be applied to the last angular coordinate, φ_9, due to its range including both $[0, \pi]$ and $(-\pi, 0)$. Although there can be a couple of ways to deal with φ_9, one possible way is to introduce a binary categorical parameter $l \in \{\text{'positive'}, \text{'negative'}\}$ that indicates the sign of φ_9. In this way, we can treat φ_9 as if it only works in the range $[0, \pi]$, like the other angular coordinate variables, and then apply the same formalism in Eq. (21) to all angular coordinate variables.

A mixed-variable problem can be generally described as:

$$\boldsymbol{x}_{opt} = \underset{\boldsymbol{x} \in \mathcal{X}}{\mathrm{argmax}}\; f(\boldsymbol{x}), \quad (23)$$

for maximizing the objective function f. The mixed-variable vector $\boldsymbol{x}$ constitutes the set $\mathcal{X} \equiv \{(\boldsymbol{y}, \boldsymbol{z}) \mid \boldsymbol{y} \in \mathcal{Y}, \boldsymbol{z} \in \mathcal{Z}\}$ representing the design space of interest, where $\boldsymbol{y} = [y_1, \ldots, y_o]$ and $\boldsymbol{z} = [z_1, \ldots, z_c]$ indicate the ordinal and categorical variables, respectively. Here $\mathcal{Y}$ and $\mathcal{Z}$ denote the ordinal and categorical spaces, respectively. Generally, each ordinal variable $y_p \in \{\mathcal{O}_1, \ldots, \mathcal{O}_\xi\}$ takes one of ξ ordinal levels (i.e. discretized numbers on the real-number line), and each categorical variable $z_q \in \{\mathcal{C}_1, \ldots, \mathcal{C}_\zeta\}$ takes one of ζ unordered categories (which by definition cannot be ordered on the real-number line).

In the context of our current riblet surface optimization problem, f corresponds to DR, $\mathcal{X}$ represents $\mathcal{D} \times \mathcal{S}$, $\boldsymbol{y}$ is a 12-dimensional ordinal variable set ($o = 12$) encompassing the 9 angular coordinate variables $\varphi_1, \cdots, \varphi_9$ and the 3 scaling and spacing variables w^+, h^+, s^+, and $\boldsymbol{z}$ is a 1-dimensional categorical variable set ($c = 1$) only including the binary parameter l. Based on the selection formalism in Eqs. (21) and (22), we choose 7 ordinal levels for the angular coordinate variables ($N_k = 6$ for all $k = 1, \cdots, 9$) and 6 ordinal levels for the scaling variables ($w_{max}^+ = h_{max}^+ = 30$, $M_w = M_h = 6$) and the spacing variable ($s_{max}^+ = 50$, $M_s = 5$), resulting in around 17 billion combinations of potential search points.

So far, we have adapted the problem of interest to the mixed-variable optimization framework. To solve this optimization problem, we employ the Mixed-Variable, Multi-Objective Bayesian Optimization (MixMOBO) algorithm [15]. This is a generalized framework capable of addressing mixed-variable problems and optimizing a noisy black-box function with a small number of function calls. The algorithm has previously been applied to optimize architected meta-materials [19, 20] and fluid structures [17, 18]. Note that MixMOBO is used here for a mixed-variable single-objective problem. Sheikh *et al.* [15] demonstrated extensive comparisons against other algorithms for such problems, revealing that MixMOBO outperforms other small-data algorithms in these scenarios.

MixMOBO, along with HedgeMO, is used in the single-objective setting for the current problem. Expected Improvement, Probability of Improvement, Upper Confidence Bound, and Stochastic Monte Carlo are the acquisition functions used for 'hedging'. Initial sample size of 10%-20% of the total iteration budget is empirically a good approximation for MixMOBO [15, 18]. The number of random evaluations to initialize the algorithm in the current case was set at 50. The interested reader is referred to Sheikh *et al.* [15] for further details on the MixMOBO algorithm.

To evaluate the efficacy of MixMOBO for our optimization problem, we optimized four different test functions in a similar design space. This helps us determine the performance of the algorithm and if our evaluation budget (i.e. the number of iteration epochs)
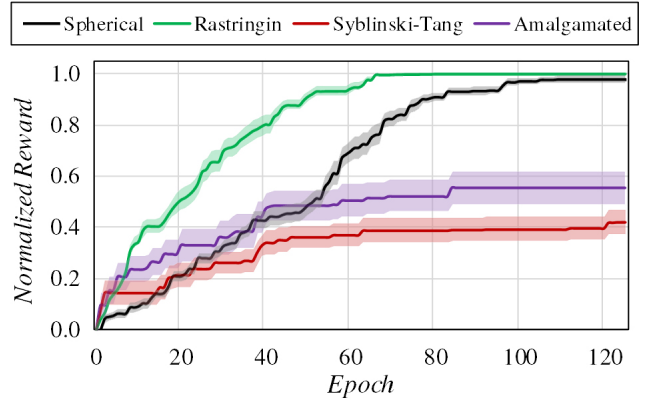

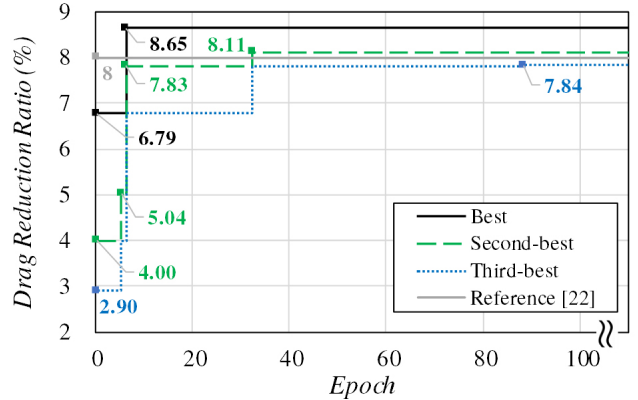**Fig. 10 Benchmarks for MixMOBO for four test functions.**

Fig. 11 Optimization history of top-three riblet surface designs at each epoch in comparison with the experimental reference [22]. Data markers and labels are drawn whenever the rank is updated. No rank change occurred after epoch #89 until the termination at epoch #125.
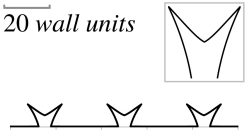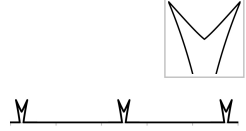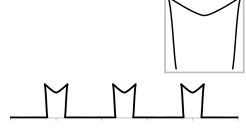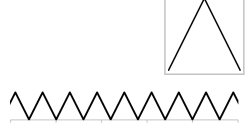
is sufficient. The test functions we used are the Spherical, Rastrigin, Syblinski-Tang, and Amalgamated functions. These functions are standard functions used to test optimization schemes [62], with the exception of the Amalgamated function, which we created to mimic an anisotropic design space. The definitions of the test functions are described in Appendix A. Similar to the design space of our problem, each test function was tested with 9 ordinal variables with 7 states each, 3 ordinal variables with 6 states each, and one qualitative variable with 2 states. To test robustness, each function was tested ten times. The mean normalized reward, defined as (current optimum - random sampling optimum)/(global optimum - random sampling optimum), is plotted with a band representing $0.2 \times$ (standard deviation). The optimization was terminated after 125 epochs, which was our prescribed computational budget, and the results are depicted in Fig. 10. It was found that MixMOBO performed well for the Rastrigin and Spherical functions in a similar design space. The performance for the Syblinski-Tang and Amalgamated functions was worse, due to their highly multimodal nature with shallow global optima, which makes them highly difficult to optimize, as can be seen from the function definitions. Overall, these results indicate that within the prescribed computational budget of 125 epochs, it is possible to obtain reasonable optimal results using MixMOBO.

5 Results

5.1 Bayesian-optimized Riblet Surface. After a total of 125 epochs of the Bayesian optimization sequence, some new riblet surface designs were found to outperform the experimental opti-

Table 3 Bayesian-optimized riblet surface design outputs.

Riblet surface	Geometry	DbM variables* (Type of morphing)	w^+	h^+	s^+	Drag reduction ratio
Type A	20 *wall units*	$\varphi_1 = \pi/6,\ \varphi_2 = 2\pi/3$ (Extrapolation)	15	10	20	8.65%
Type B		$\varphi_1 = \pi/6,\ \varphi_2 = 5\pi/6$ (Extrapolation)	5	10	40	8.11%
Type C		$\varphi_1 = \pi/6,\ \varphi_2 = \pi/3,$ $\varphi_3 = 5\pi/6,\ \varphi_4 = 2\pi/3,$ $\varphi_5 = 5\pi/6,\ \varphi_6 = 2\pi/3$ (Extrapolation)	10	15	20	7.84%
Reference [21, 22]		$\varphi_1 = \pi/2$ (Baseline #2)	12	12	0	8%

* All unspecified variables are 0.

mum, with a drag reduction (DR) of 8% [21, 22]. These designs were investigated and compared to the conventional designs shown in Fig. 3. The history of the Bayesian optimization sequence is depicted in Fig. 11 and shows the improvement in DR of the top three designs. The best riblet surface design, with a DR of 8.65%, appeared early in the optimization process (epoch 7) and maintained its position until the termination, implying the validity of the optimization. The second-best design also slightly surpassed the reference in terms of DR. Although the third-best design did not surpass the reference nominally, it was considered for further analysis due to the uncertainty of the reference value of 8% DR [21], which may have arisen from errors in drag measurement.

The top three riblet surface designs with a DR of 8.65%, 8.11% and 7.84% are presented in detail in Table 3, including their geometry and scale information. Henceforth, these designs are referred to as type A, type B, and type C, respectively. Although all of the Bayesian-optimized riblet surface types are created from different combinations of the DbM variables, they are commonly characterized by two prominent design features: (i) a tapering neck, and (ii) a notch top. It is noteworthy that the tapering neck feature was *explicitly* desired to be present in the design space for novelty through our original baseline designs (#9, #10). However, these DbM baseline shapes did not participate in the construction of the current optimal designs (i.e. $\omega_9 = \omega_{10} = 0$ because $\varphi_8 = 0$). Instead, the tapering-neck feature was obtained from the extrapolative searches during the DbM process. This confirms the strength of DbM to treat such radical designs outside the convention even without specification in the baseline selection. The reason why the original baseline designs were entirely dropped out is believed to be because all the optima commonly possess the notch-top feature as well, while the original baseline designs do not. They have either flat (#9) or round (#10) riblet tops, which may not be suitable to form a notch.

With these two common features combined, all Bayesian-optimized riblet surfaces exhibit a *spiky* tip geometry. A downside of a tapering neck or a notch top is the manufacturing challenge due to the negative taper or overhang, as additive manufacturing is assumed to be the primary fabrication method in this study. However, as the geometry is identical throughout the flow direction, printing direction-based multiscale stereolithography may be utilized to create micro-sized identical geometry even with overhang [14].

When it comes to riblet scaling, the optimal riblet shapes are scaled to a maximum of 15 wall units in width or height. This result agrees with previous findings that the optimal riblet size is $O(15)$ in wall units [22, 38]. Unlike the reference optimum of repeating triangular riblets with zero spacing, known as V-grooves, the current optimal riblet surface designs arrange the riblets in a relatively sparse manner. For example, type B has a spacing of 40 wall units between neighboring riblets, meaning that a large portion of this riblet surface remains flat. This sparse configuration is favorable for additive manufacturing on flat walls, as it requires less material usage. If we quantitatively consider the fraction of the void in the riblet region ($y^+ \leq h^+$), or the void fraction, a reduction in material usage becomes more evident. For types A, B, and C, the void fractions are 84%, 96%, and 75%, respectively, in contrast to the reference case where it is only 50%.

As a result, we believe that the Bayesian-optimized riblet surface designs we have computationally proposed are not only geometrically novel but also competent to be manufactured using emerging 3D printing techniques. Speaking of performance, the nominal improvement in DR of the best design, calculated as $(8.65 - 8)/8 = 8.1\%$, is significant enough to hold practical relevance. Furthermore, the geometric resemblance among the top three designs indicates the robustness of their shared features in contributing to drag reduction.

5.2 Flow Structure Near Riblets. Although the main focus of this study is the computational parametric optimization of riblet surface for drag reduction, a brief analysis of the flow structures is conducted here. The analysis presented here is preliminary, yet still has significance in comprehending the physical mechanism correlating the currently obtained designs, which especially reveal the common features, with the reduction in drag forces. However, too in-depth analysis is avoided here because it would be outside the scope of this paper. A more profound analysis will follow after higher resolution simulations and further experiments for design validation are conducted in the future, as the current LES calcula-
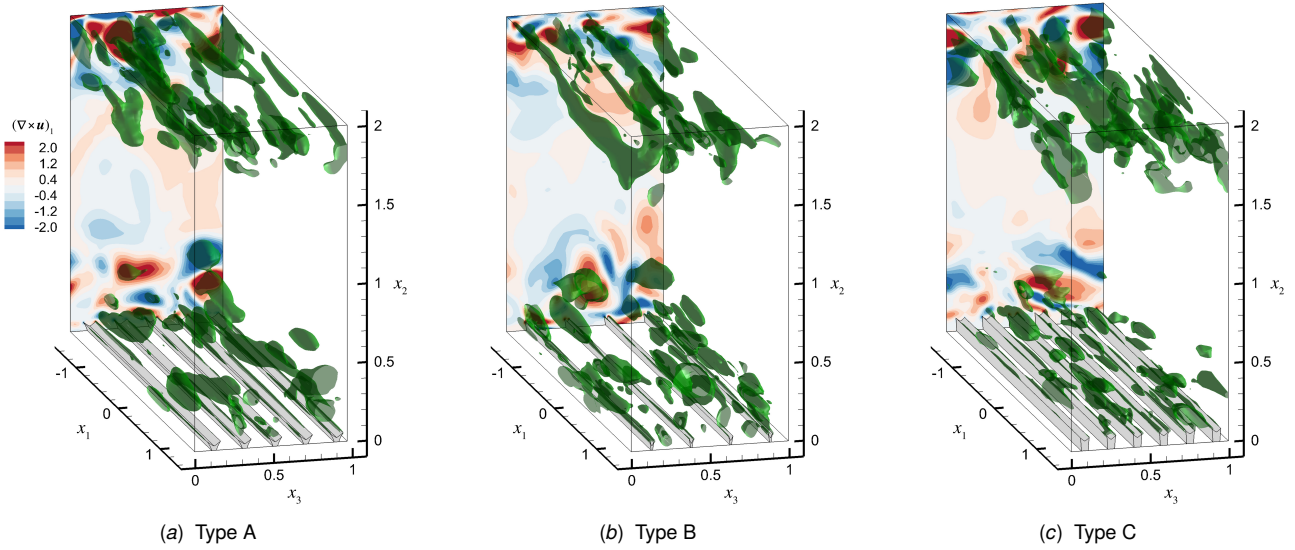
Fig. 12 **Instantaneous flow fields of top three riblet surface designs where turbulence structures are visualized using the lambda-2 iso-surface of $\lambda_2 = -1$ in green. At the back plane, an auxiliary contour of x_1-vorticity is shown. For dimensionless scaling, the channel half-height ς and the bulk velocity U_b are used.**

tions had to trade off some time-efficiency for optimization to some extent. Note that the observations made here are comprehensively considered later to discuss how our proposed designs' common features potentially contribute to drag reduction (see §6.1).

In comparison to several pieces of literature, our LES results are believed to be in good agreement with previous observations regarding the passive drag reduction of a riblet surface. One of the kinetic influences of riblets on a channel wall is that they hinder the local motion of the flow closest to the wall, especially in the cross-flow direction, resulting in a thickening of the viscous sublayer in the turbulent boundary layer [23, 63]. The restriction in the spanwise movement may lead to a weak "burst" that generates turbulence near the wall [8], considered one of the main sources of skin friction.

3D instantaneous turbulent flow fields over all three types of Bayesian-optimized riblet designs are depicted in Fig. 12. All fields were captured near the end of the simulation ($t = 195$), ensuring that they are fully developed and turbulent. Green surfaces represent the λ_2 iso-surface of $\lambda_2 = -1$, often used to detect where vortex core lines are present in a given fluid velocity field [64]. Auxiliary contours of the x_1-vorticity, indicating the secondary flow motion in the x_2-x_3 plane, are also drawn. It is noted that in this figure, the bulk streamwise mean velocity U_b is substituted for the shear velocity u_τ for velocity scaling. Since u_τ was set so that $Re_\tau = 180$ in the flat channel, the exact shear velocity in each riblet case may slightly differ from u_τ defined in the flat case. To reduce complexity and ensure a fair comparison, we use U_b that keeps all cases at the same dimensionless volume flow rate of $2X_3$.

In Fig. 12, it is clear that on the riblet surface, turbulent vortical motion rarely intrudes into the riblet zone, whereas on the flat surface, such vortical motion easily reaches the near-wall region. Therefore, the riblet design significantly protects the majority of the surface from the impact of turbulence. This supports the argument that riblets hinder nearby cross-flow motion. Additionally, concentrated vortex lines are often detected at the spiky riblet tips because the flow experiences a drastic change in orientation around these sharp points. Such vorticity concentration at sharp riblet peaks was similarly observed in conventional triangular riblet cases [25, 33] and therefore appears rational. The configuration of the streamwise vortices residing above the riblet tips (not in the notch valleys) also appears to be similar to the drag-reducing case found experimentally [65]. However, due to the relatively sparse distribution of grids in the x_1-direction, the current visualization may not accu-

rately express more precise 3D turbulent flow structures. Later, a higher-resolution simulation should be necessary for more robust validation of the proposed designs.

To check the turbulence statistics, we took the time average from $t = 32.5$ to $t = 195$ of each simulation and obtained the mean and fluctuation flow fields. In Fig. 13, contours of the mean pressure $\tilde{p}$, x_1-vorticity $(\nabla \times \boldsymbol{u})_1$, and streamwise velocity u_1 are given at the middle cross-section (i.e., $x_1 = 0$ in Fig. 12). Only two riblet patterns in the computational domain are shown here for the sake of simplicity. It is commonly observed that the riblet structures have only a local influence on the flow near them. The pressure contours reveal that the negative pressure area above the riblets has a smaller absolute value than that below the top flat surface. This indicates that the net vertical momentum transport is weakened due to the riblets, which is presumably the result of hindrance in the cross-flow direction.

A more distinct difference in the mean flow fields over the riblet and flat surfaces can be seen in the x_1-vorticity contour. We can detect a horizontal line of paired vortices right above the riblet tips. As seen in the instantaneous fields, highly concentrated vortices are found at the tips. In addition, larger vortices, whose size depends on the riblet spacing, also appear around them. The layer of streamwise vortices over the riblets may serve as an impediment for low-speed fluid parcels near the wall (particularly within the riblet spacing) from being lifted upward, which relates to the vortex-surface interaction proposed from the V-groove surface examination [66]. Unlike the V-groove surface, where no spacing exists between the patterns, the current riblet surfaces offer more space for the flow to stay within the spacing of lower speed with less turbulence. We affirm that this provides a unique practical advantage to our designs in terms of turbulent drag reduction.

The retardation of the streamwise velocity within the spacing due to the riblets is shown in Fig. 14. Two mean streamwise profiles in red and black are obtained through the center of the riblet spacing and past the riblet tip, respectively (one may refer to Fig. 13 for the locations). The mean streamwise velocity slows down notably as the flow approaches the riblets, which potentially contributes to a decrease in skin friction. The centerline profile changes relatively little compared to the flat surface counterpart, especially when the spacing is large (e.g., type B). However, we next show that the whole spacing region benefits from a reduction in turbulence due to the riblets.

In Fig. 15, contours of the root-mean-square (RMS) fluctuation
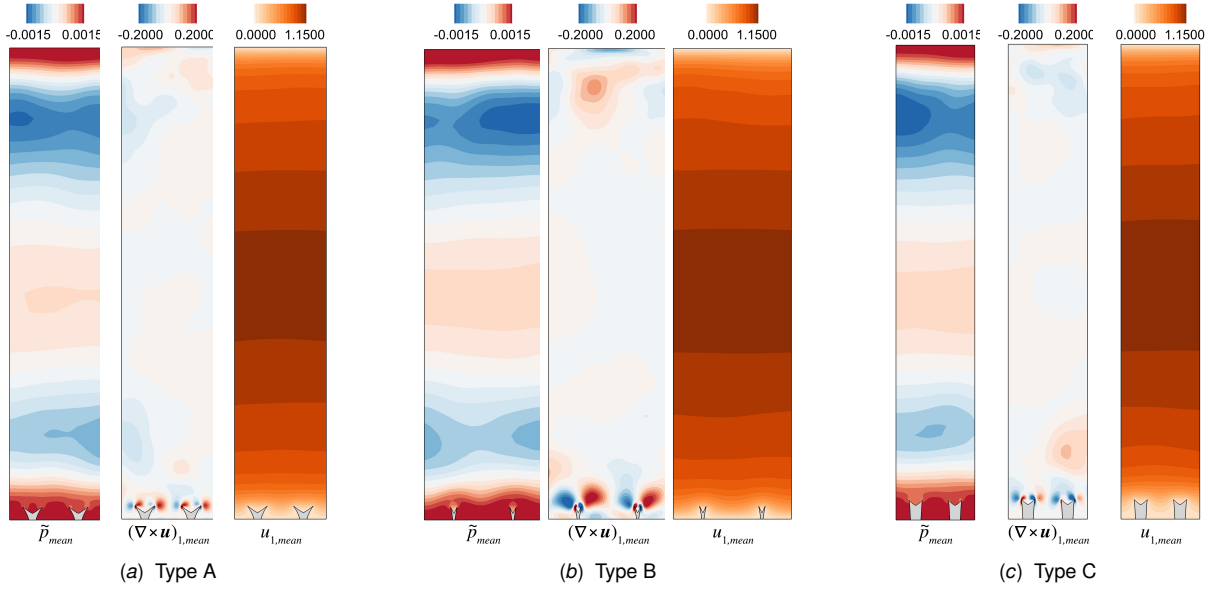
Fig. 13 Contours of mean pressure, x_1-vorticity and streamwise velocity at the channel section perpendicular to the flow direction, representing time-averaged flow characteristics. For dimensionless scaling, the fluid density ρ and the bulk velocity U_b are used.
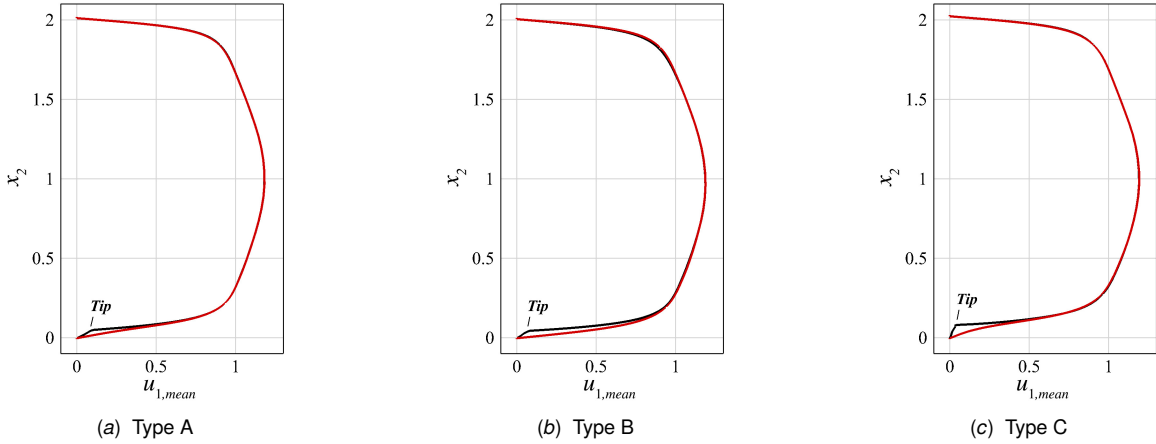
Fig. 14 Mean streamwise velocity profiles (red) through the center of riblet spacing and (black) past the riblet tip. For dimensionless scaling, the channel half-height ς and the bulk velocity U_b are used.

pressure $\tilde{p}'_{RMS}$, x_1-vorticity $(\nabla \times \boldsymbol{u})'_{1,RMS}$, streamwise velocity $u'_{1,RMS}$ and turbulent kinetic energy (TKE) are displayed. Note that for a scalar physical quantity, say α, its RMS fluctuation quantity, α'_{RMS}, is calculated as

$$\alpha'_{RMS} = \sqrt{(\alpha^2)_{mean} - (\alpha_{mean})^2}, \qquad (24)$$

and TKE is obtained as follows:

$$\text{TKE} = \frac{1}{2} \sum_{i=1}^{3} {u'_{i,RMS}}^2. \qquad (25)$$

The TKE contours clearly reveal that the local flow field around the riblets, including the spacing region, is generally less turbulent. This confirms the widespread consensus that riblets influence the near-wall turbulent structure [67]. The other contours of the RMS fluctuation quantities similarly show a reduction in turbulence intensity near the wall; turbulent fluctuation is generally found to be weaker compared to what can be observed near the top flat surface, consistent with previous findings [8, 68]. The only exception

is the RMS fluctuation vorticity around the spiky tips of the riblets. Such intense fluctuation implies that the riblet tips are exposed to relatively high levels of turbulent shear stress and may be structurally vulnerable to wear as a result, a consideration that should be carefully addressed in future manufacturing practices.

6 Discussion

6.1 Drag Reduction Mechanisms. As the present optimization resulted in geometrically similar riblet surfaces, it is meaningful to discuss the physical mechanism of how these spaced and spiky riblets are effective in reducing drag. Fig. 16 demonstrates a schematic diagram of the spiky riblet surface that we have proposed and the nearby flow. From the time-averaged flow fields of all three optimal riblet surface designs, it is commonly observed that there is a layer of periodic streamwise vortex pairs right above the riblet tips (see Fig. 13), and turbulence is overall suppressed in the riblet area, increasing steeply as soon as it leaves the riblets (see Fig. 15). This circulation zone functions as a division between the main part of the flow in the channel center and the flow below the riblets, characterized by weak turbulence and relatively low speed.

| (a) Type A | (b) Type B | (c) Type C |
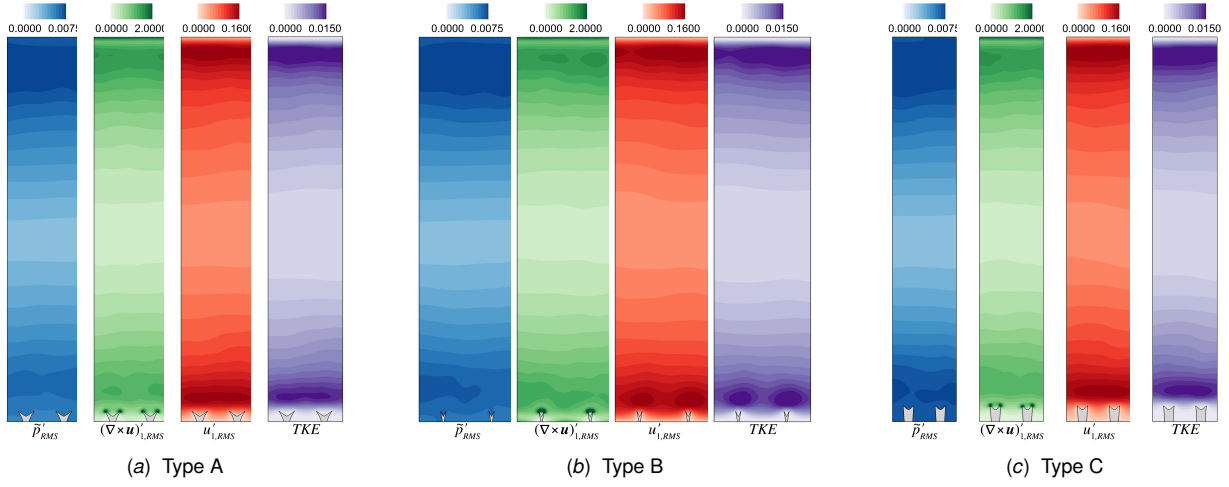
Fig. 15 Contours of root-mean-square (RMS) fluctuation pressure, x_1-vorticity, streamwise velocity and turbulent kinetic energy (TKE) at the channel section perpendicular to the flow direction, representing turbulent flow characteristics. For dimensionless scaling, the fluid density ρ and the bulk velocity U_b are used.
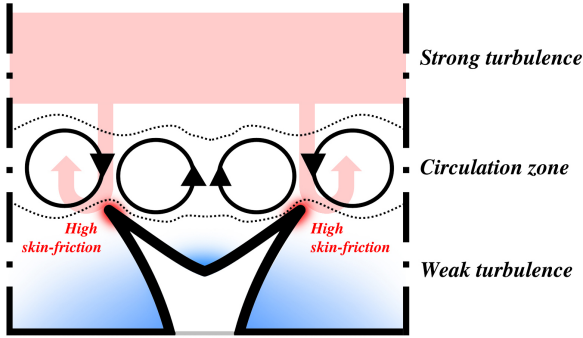
Fig. 16 Schematic diagram of a potential mechanism for turbulent drag reduction by our new riblet surface designs.

We propose that the presence of the circulation zone serves two major roles. First, it restricts the incursion of strong turbulence into the lower layer. In other words, the vortex arrangement in the circulation zone reduces the occurrence of downwash and ejection motions. In particular, the downwash motion of strong turbulence is mainly directed towards the riblet tips. Linking to our observation of intense vorticity fluctuation at the riblet tips, this implies high skin friction only concentrated in this highly limited area. The concentration of friction can contribute to drag reduction because the remaining large area benefits from relatively low skin friction. Second, thanks to the location of the circulation zone, the spacing between the riblets remains mostly weakly turbulent and low-speed. The lower riblet surface as well as the bottom flat wall should, therefore, experience less turbulent shear stress. Although this comes at the expense of an increase in the wetted area, like all other riblets, the relatively sparse riblet configuration of our proposed designs is believed to be helpful in mitigating the counter-effect.

It should be noted that the physical mechanisms described above for riblet drag reduction are, by and large, still hypothetical and need further corroboration. They are mostly based on the time-averaged flow fields, and the instantaneous flow interaction has not been taken into account yet. To relate to the previously suggested riblet drag reduction mechanisms [8, 23, 33, 63], an in-depth investigation of the flow evolution over time should be conducted with high resolution to gain a clear understanding of turbulent structures.

Algorithm 1 DbM + LES/IB Riblet Drag Reduction Evaluation

1: **Constants:**
   N baseline riblet shapes $(\mathcal{R}_i)_{i=1:N}$,
   Reynolds number Re_τ,
   Computational domain $[-X_1/2, X_1/2] \times [0, X_2] \times [0, X_3]$
   and grid $(x_1^0, \cdots, x_1^{N_1}) \times (x_2^0, \cdots, x_2^{N_2}) \times (x_3^0, \cdots, x_3^{N_3})$
   Total time advancement T_f
2: **Inputs:**
   N Design-by-Morphing weights $(\omega_i)_{i=1:N}$
   or $(N-1)$ angular coordinates $(\varphi_i)_{i=1:N-1}$,   ▷ Eq. (9)
   3 scaling and spacing parameters (w^+, h^+, s^+)
3: **Initialize:**
   $t = 0$; $\boldsymbol{u} = \boldsymbol{0}$; $\tilde{p} = 0$; $\Sigma D_r = 0$; $\Sigma D_f = 0$
4: Morph $\mathcal{M} = \text{morph}\left((\omega_i)_{i=1:N}; (\mathcal{R}_i)_{i=1:N}\right)$ ▷ Eq. (5)
5: **if** $\mathcal{M}$ is a self-intersecting curve **then**
6:   **return** $DR = 0$ ▷ Termination due to shape invalidity
7: **end if**
8: Scale $\mathcal{M}' = \text{scale}(\mathcal{M}, \ x_{2,\max} = h^+/Re_\tau, \ x_{3,\max} = w^+/Re_\tau)$
9: Space & patternize $\{\mathcal{M}'_i\}_{i=0:\infty}$
   where $\mathcal{M}'_i = \text{translate}(\mathcal{M}', \ x_1 = x_1 - i \cdot (w^+ + s^+)/Re_\tau)$
10: **while** $t \le T_f$ **do**
11:   **for** each computation cell $\mathcal{C}_{ijk}$ **do**
12:     **if** $\mathcal{C}_{ijk}$ captures $\{\mathcal{M}'_i\}_{i=0:\infty}$ **then**   ▷ Fig. 8
13:       Calculate momentum forcing
        $\boldsymbol{f}_{ijk} = \text{mmt\_forcing}(x_1^i, x_2^j, x_3^k; \boldsymbol{u}, \tilde{p}, \{\mathcal{M}'_i\}_{i=1:\infty})$
14:       Calculate mass source/sink
        $m_{ijk} = \text{mss\_source}(x_1^i, x_2^j, x_3^k; \boldsymbol{u}, \tilde{p}, \{\mathcal{M}'_i\}_{i=1:\infty})$
15:     **else**
16:       $\boldsymbol{f}_{ijk} = \boldsymbol{0}$; $m_{ijk} = 0$
17:     **end if**
18:     Calculate subgrid-scale stress   ▷ Eq. (14)
        $\boldsymbol{\tau}_{ijk} = \text{sgs\_stress}(x_1^i, x_2^j, x_3^k; \boldsymbol{u}, \tilde{p}, \{\mathcal{M}'_i\}_{i=1:\infty})$
19:   **end for**
20:   CFL time step $\Delta t = 3/\left(\sum_{i=1}^3 u_i/\Delta x_i\right)_{\max}$
21:   Update $(\boldsymbol{u}, \tilde{p}) = \text{finite\_volume}(\boldsymbol{u}, \tilde{p}, \boldsymbol{f}, m, \tau, \Delta t)$ ▷ Ref. [40]
22:   **if** $U_b/U_{b,\text{reference}}$ reaches 90% **then**
23:     Trigger instability $\boldsymbol{u} = \boldsymbol{u} + \delta\boldsymbol{u}_{\text{pert}}$ ▷ Ref. [49]
24:   **end if**
25:   **if** $\boldsymbol{u}$ is fully developed **then**
26:     $\Sigma D_r = \Sigma D_r + D_r \cdot \Delta t$; $\Sigma D_f = \Sigma D_f + D_f \cdot \Delta t$ ▷ Eq. (19)
27:   **end if**
28:   $t = t + \Delta t$
29: **end while**
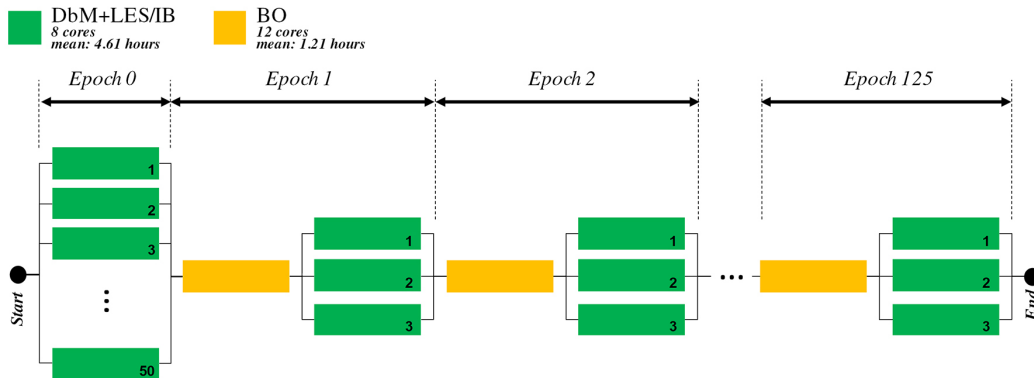30: **return** $DR = \max(1 - \Sigma D_r/\Sigma D_f, \ 0)$ ▷ Normal termination

---

Fig. 17 Task flowchart for overall optimization. Each task uses multi-core parallelism and tasks in the same column are executed in parallel. The computation was done using SDSC EXPANSE (AMD EPYC 7742 CPU, 4608 GFLOPS in total) [69].

6.2 Optimization Scheme. Our computational optimization process consists of three numerically important parts, as shown in Fig. 2, including Design-by-Morphing (DbM), Large Eddy Simulation (LES), and Bayesian Optimization (BO). From the optimization perspective, DbM and LES can be linked together to form a consolidated algorithm that serves as a 'black-box' function. The optimizer only needs to know the parametric inputs of the function (DbM weights, scaling, and spacing parameters) and its output (drag reduction ratio DR). Therefore, the optimization process can be simplified to a sequential iteration of two algorithms: black-box function evaluation and Bayesian optimum guess (or sampling). The former procedure, explained in §2 and §3 and summarized in Algorithm 1: DbM + LES/IB, emphasizes the importance of the Immersed-Boundary (IB) method in the algorithm. It enables the algorithm to run with a constant grid setup regardless of riblet surface designs. On the other hand, the latter algorithm uses DbM + LES/IB for sampling and conducts estimation through BO. A detailed algorithmic explanation is given in Sheikh *et al.* [18] for reference.

Using this two-step simplification, the task flowchart for the overall optimization is shown in Fig. 17 to analyze the practicality of the present optimization. For efficiency, we applied parallelism to each task and to the whole task flow to the best extent possible. The DbM+LES/IB task, using 8 cores for each, took an average of 4.61 hours, and the BO task, using 12 cores for each, finished in an average of 1.21 hours. As a result, it took 5.82 hours to complete one epoch in practice, meaning that the current optimization attempt (see Fig. 11) achieved the best riblet design (type A) within 2 days. Even without considering parallelism, the total core hours for all DbM+LES/IB and BO tasks are 4.61 hours $\times$ 8 cores $\times$ $(50 + 3 \times 125)$ tasks $= 1.567 \times 10^4$ core hours and 1.21 hours $\times$ 12 cores $\times$ (1×125) tasks $= 1.815 \times 10^3$ core hours, respectively. The time breakdown analysis shows that the evaluation, despite involving LES, can be performed in 8.6 times the main optimization run time. Despite the conventional belief that LES is not suitable for optimization due to its generally large computational expense, our optimization highlights the possibility that LES can be favorably considered as part of fluid engineering optimization tools with the advancement in modern computing power.

7 Conclusion

The advancement of additive manufacturing has made it possible to consider more complex riblet surface structures for drag reduction beyond simple geometric shapes on a flat surface. With this motivation, we present a computational approach that combines Design-by-Morphing (DbM), Large Eddy Simulation (LES), and Bayesian Optimization (BO) to identify and optimize new riblet surface designs in a channel flow for the purpose of drag reduction. The approach begins by using DbM to generate an ex-

tensive and continuous design space involving novel riblet surface designs by morphing existing ones not only interpolatively but also extrapolatively. Following the scaling and spacing of riblets, their drag-reducing capabilities are numerically evaluated using LES, which incorporates the Immersed-Boundary (IB) method. This allows every riblet surface design to be simulated under the same computational grid condition, thereby avoiding grid dependency. By treating DbM and LES/IB as black-box functions, the mixed-variable BO algorithm, MixMOBO, is used to optimize the riblet surface geometry for maximum drag reduction.

Taking into account our computing budget and the performance test of the BO algorithm, we carried out a total of 125 epochs (cycles) of the optimization process under the turbulent flow condition of $Re_\tau = 180$. As a result, we identified three optimal riblet surface designs that performed as well as or better than the reference triangular riblets for drag reduction of 8%, with respective values of 8.65%, 8.11%, and 7.84%. All three Bayesian-optimized designs showed riblet sizes in $O(15)$ in wall units, which agrees with previous experimental studies, and relatively large spacing compared to conventional designs. This spacing is favorable, as it indicates less material usage from the perspective of additive manufacturing. Interestingly, they all featured spiky tips with notches on the riblets. This feature is believed to be physically beneficial in creating a circulation zone right above the riblet tips, which helps protect most of the channel wall region from experiencing large skin friction due to high turbulent shear stress. However, further investigation through experiments and high-resolution simulations will be necessary to validate the precise drag reduction mechanism.

By using parallel computing with a moderate number of cores, either 8 or 12, we could conduct our computational optimization process within a reasonable physical time frame. Although we heavily relied on LES for evaluation, which is often considered computationally expensive, the physical time required for a DbM+LES/IB evaluation task was only about four times longer than that for a single BO sampling task. Moreover, even without considering parallelism, the resource usage ratio between the two tasks was less than 10. These time breakdowns demonstrate that LES in combination with BO can be practically used for engineering optimization problems, especially when the reliability of computational designs needs to be ensured before prototyping or realization.

Appendix A: Benchmark Test Functions

In what follows, we present the definitions of four test functions used to benchmark the Bayesian optimization setup in the current study (see Fig. 10 in §4). All the functions are multivariate with respect to d independent variables $\boldsymbol{x} = (x_1, x_2, \ldots, x_d)$. The number of independent variables d can be chosen arbitrarily.

The *Spherical* function f_S is a convex function defined as

$$f_S(\boldsymbol{x}) = -\sum_{i=1}^{d} x_i^2, \tag{A1}$$

where $x_i \in (-10, \ 10)$ for all i. The *Rastringin* function f_R is a non-convex function defined as

$$f_R(\boldsymbol{x}) = -\sum_{i=1}^{d} [10 + x_i^2 - 10\cos(2\pi x_i)], \tag{A2}$$

where $x_i \in (-5.12, \ 5.12)$ for all i. The *Syblinski-Tang* function f_{ST} is a non-convex function defined as

$$f_{ST}(\boldsymbol{x}) = -\sum_{i=1}^{d} \frac{(x_i^4 - 16x_i^2 + 5x_i)}{2}, \tag{A3}$$

where $x_i \in (-5, \ 5)$ for all i. Lastly, the *Amalgamated* function f_A is a non-convex, non-uniform and anisotropic function defined as

$$f_A(\boldsymbol{x}) = -\sum_{i=1}^{d} g(x_i), \tag{A4}$$

where, using $k \equiv \mathrm{mod}(i - 1, \ 7)$, for all i:

$$g(x_i) = \begin{cases} -\sin(x_i) & x_i \in (0, \ \pi) \\ & \text{if } k = 0, \\ (x_i^4 - 16x_i^2 + 5x_i)/2 & x_i \in (-5, \ 5) \\ & \text{if } k = 1, \\ x_i^2 & x_i \in (-10, \ 10) \\ & \text{if } k = 2, \\ [10 + x_i^2 - 10\cos(2\pi x_i)] & x_i \in (-5.12, \ 5.12) \\ & \text{if } k = 3, \\ [100(x_i - x_{i-1}^2)^2 + (1 - x_i)^2] & x_i \in (-2, \ 2) \\ & \text{if } k = 4, \\ -|\cos(x_i)| & x_i \in (-\pi/2, \ \pi/2) \\ & \text{if } k = 5, \\ x_i & x_i \in (-30, \ 30) \\ & \text{if } k = 6. \end{cases}$$

For ordinal and categorical variables, the range for each test function is equally discretized for each variable. The details of the test functions, except the *Amalgamated* function, can be found in Tušar [62]. All test functions presented above have known global maxima. We produced the *Amalgamated* function, a piece-wise function formed from commonly used analytical test functions with different features. The *Amalgamated* function is non-convex and anisotropic (as is our design space for the current problem), unlike the other test functions listed here, which are isotropic. The other test functions are commonly used for testing optimization algorithms [20].

References

[1] Yu, C., Liu, M., Zhang, C., Yan, H., Zhang, M., Wu, Q., Liu, M., and Jiang, L., 2020, "Bio-inspired drag reduction: From nature organisms to artificial functional surfaces," Giant, **2**, p. 100017.

[2] Liu, G., Yuan, Z., Qiu, Z., Feng, S., Xie, Y., Leng, D., and Tian, X., 2020, "A brief review of bio-inspired surface technology and application toward underwater drag reduction," Ocean Engineering, **199**, p. 106962.

[3] Ball, P., 1999, "Engineering Shark skin and other solutions," Nature, **400**(6744), pp. 507–509.

[4] Bhasin, D., McAdams, D. A., and Layton, A., 2021, "A Product Architecture-Based Tool for Bioinspired Function-Sharing," Journal of Mechanical Design, **143**(8), p. 081401.

[5] Ott, J., Lazalde, M., and Gu, G. X., 2020, "Algorithmic-driven design of shark denticle bioinspired structures for superior aerodynamic properties," Bioinspiration & Biomimetics, **15**(2), p. 026001.

[6] Parfitt, A. R. and Vincent, J. F. V., 2005, "Drag reduction in a swimming humboldt penguin, Spheniscus humboldti, when the boundary layer is turbulent," Journal of Bionic Engineering, **2**(2), pp. 57–62.

[7] Bannasch, R., 1995, *Hydrodynamics of penguins–an experimental approach*, Surrey Beatty & Sons, Chipping Norton, NSW, Chap. 9, pp. 141–176.

[8] Choi, K.-S., 1989, "Near-wall structure of a turbulent boundary layer with riblets," Journal of Fluid Mechanics, **208**, pp. 417–458.

[9] Bixler, G. D. and Bhushan, B., 2013, "Fluid Drag Reduction with Shark-Skin Riblet Inspired Microstructured Surfaces," Advanced Functional Materials, **23**(36), pp. 4507–4528.

[10] Han, M., Lim, H., Jang, Y.-G., Lee, S., and Lee, S.-J., 2003, "Fabrication of a micro-riblet film and drag reduction effects on curved objects," *12th International Conference on Solid-State Sensors, Actuators and Microsystems. Digest of Technical Papers (Cat. No.03TH8664)*, Vol. 1, IEEE, Boston, Massachusetts, USA, 08-12 June 2003, pp. 396–399, doi: 10.1109/SENSOR.2003.1215337.

[11] Sundaram, S., Viswanath, P. R., and Rudrakumar, S., 1996, "Viscous drag reduction using riblets on NACA 0012 airfoil to moderate incidence," AIAA Journal, **34**(4), pp. 676–682.

[12] Dai, W., Alkahtani, M., Hemmer, P. R., and Liang, H., 2019, "Drag-reduction of 3D printed shark-skin-like surfaces," Friction, **7**(6), pp. 603–612.

[13] Wen, L., Weaver, J. C., and Lauder, G. V., 2014, "Biomimetic shark skin: design, fabrication and hydrodynamic function," Journal of Experimental Biology, **217**(10), pp. 1656–1666.

[14] Li, Y., Mao, H., Hu, P., Hermes, M., Lim, H., Yoon, J., Luhar, M., Chen, Y., and Wu, W., 2019, "Bioinspired functional surfaces enabled by multiscale stereolithography," Advanced Materials Technologies, **4**(5), p. 1800638.

[15] Sheikh, H. M. and Marcus, P. S., 2022, "Bayesian optimization for mixed-variable, multi-objective problems," Structural and Multidisciplinary Optimization, **65**(11), p. 331.

[16] Oh, S., Jiang, C.-H., Jiang, C., and Marcus, P. S., 2018, "Finding the optimal shape of the leading-and-trailing car of a high-speed train using design-by-morphing," Computational Mechanics, **62**(1), pp. 23–45.

[17] Sheikh, H. M., Lee, S., Wang, J., and Marcus, P. S., 2023, "Airfoil optimization using Design-by-Morphing," Journal of Computational Design and Engineering, **10**(4), pp. 1443–1459.

[18] Sheikh, H. M., Callan, T. A., Hennessy, K. J., and Marcus, P. S., 2022, "Optimization of the Shape of a Hydrokinetic Turbine's Draft Tube and Hub Assembly Using Design-by-Morphing with Bayesian Optimization," Computer Methods in Applied Mechanics and Engineering, **401**, p. 115654.

[19] Vangelatos, Z., Sheikh, H. M., Marcus, P. S., Grigoropoulos, C. P., Lopez, V. Z., Flamourakis, G., and Farsari, M., 2021, "Strength through defects: A novel Bayesian approach for the optimization of architected materials," Science Advances, **7**(41), p. eabk2218.

[20] Sheikh, H. M., Meier, T., Blankenship, B., Vangelatos, Z., Zhao, N., Marcus, P. S., and Grigoropoulos, C. P., 2022, "Systematic design of Cauchy symmetric structures through Bayesian optimization," International Journal of Mechanical Sciences, p. 107741.

[21] Walsh, M., 1982, "Turbulent boundary layer drag reduction using riblets," *20th Aerospace Sciences Meeting*, American Institute of Aeronautics and Astronautics, Orlando, Florida, USA, 11-14 January 1982, doi: 10.2514/6.1982-169.

[22] Walsh, M., 1986, "Riblets For Aircraft Skin-Friction Reduction," NASA Langley Research Center, Hampton, Virginia, https://ntrs.nasa.gov/citations/19880005573

[23] Bechert, D. W., Bruse, M., Hage, W., Van der Hoeven, J. G. T., and Hoppe, G., 1997, "Experiments on drag-reducing surfaces and their optimization with an adjustable geometry," Journal of Fluid Mechanics, **338**, pp. 59–87.

[24] Bechert, D. W., Bruse, M., Hage, W., and Meyer, R., 2000, "Fluid Mechanics of Biological Surfaces and their Technological Application," Naturwissenschaften, **87**(4), pp. 157–171.

[25] Bai, X., Zhang, X., and Yuan, C., 2016, "Numerical Analysis of Drag Reduction Performance of Different Shaped Riblet Surfaces," Marine Technology Society Journal, **50**(1), pp. 62–72.

[26] Heidarian, A., Ghassemi, H., and Liu, P., 2018, "Numerical Analysis of the Effects of Riblets on Drag Reduction of a Flat Plate," Journal of Applied Fluid Mechanics, **11**(3), pp. 679–688.

[27] Ao, M., Wang, M., and Zhu, F., 2021, "Investigation of the Turbulent Drag Reduction Mechanism of a Kind of Microstructure on Riblet Surface," Micromachines, **12**(1), p. 59.

[28] Klocke, F., Feldhaus, B., and Mader, S., 2007, "Development of an incremental rolling process for the production of defined riblet surface structures," Production Engineering, **1**(3), pp. 233–237.

[29] Gao, X., Zhu, G., Wang, H., Guo, N., and Wang, Z., 2021, "Research on micro riblets rolling process based on uncertainty analysis," Materials Today Communications, **27**, p. 102302.

[30] Blumenson, L. E., 1960, "A Derivation of n-Dimensional Spherical Coordinates," The American Mathematical Monthly, **67**(1), pp. 63–66.

[31] GEOS contributors, 2021, *GEOS coordinate transformation software library*, Open Source Geospatial Foundation, https://libgeos.org/

[32] Walsh, M. and Lindemann, A., 1984, "Optimization and application of riblets for turbulent drag reduction," *22nd Aerospace Sciences Meeting*, American Institute of Aeronautics and Astronautics, Reno, Nevada, USA, 09-12 January 1984, doi: 10.2514/6.1984-347.

[33] Choi, H., Moin, P., and Kim, J., 1993, "Direct numerical simulation of turbulent flow over riblets," Journal of Fluid Mechanics, **255**, pp. 503–539.

[34] García-Mayoral, R. and Jiménez, J., 2011, "Drag reduction by riblets," Philosophical Transactions of the Royal Society A: Mathematical, Physical and Engineering Sciences, **369**(1940), pp. 1412–1427.

[35] Martin, S. and Bhushan, B., 2016, "Fluid flow analysis of continuous and segmented riblet structures," RSC Advances, **6**(13), pp. 10962–10978.

[36] Lee, S. and Hwang, W., 2019, "Development of an efficient immersed-boundary method with subgrid-scale models for conjugate heat transfer analysis using large eddy simulation," International Journal of Heat and Mass Transfer, **134**, pp. 198–208.

[37] Baek, S., Lee, S., Hwang, W., and Park, J. S., 2019, "Experimental and Numerical Investigation of the Flow in a Trailing Edge Ribbed Internal Cooling Passage," Journal of Turbomachinery, **141**(1), pp. 1–9.

[38] Abdulbari, H. A., Mahammed, H. D., and Hassan, Z. B. Y., 2015, "Bio-Inspired Passive Drag Reduction Techniques: A Review," ChemBioEng Reviews, **2**(3), pp. 185–203.

[39] Choi, H. and Moin, P., 2012, "Grid-point requirements for large eddy simulation: Chapman's estimates revisited," Physics of Fluids, **24**(1), p. 011702.

[40] Kim, J., Kim, D., and Choi, H., 2001, "An Immersed-Boundary Finite-Volume Method for Simulations of Flow in Complex Geometries," Journal of Computational Physics, **171**(1), pp. 132–150.

[41] Kim, J., Moin, P., and Moser, R., 1987, "Turbulence statistics in fully developed channel flow at low reynolds number," Journal of Fluid Mechanics, **177**(13800), pp. 133–166.

[42] Tsukahara, T., Seki, Y., Kawamura, H., and Tochio, D., 2005, "DNS of turbulent channel flow at very low Reynolds numbers," *Proceeding of Fourth International Symposium on Turbulence and Shear Flow Phenomena*, Begellhouse, Williamsburg, Virginia, USA, 27-29 June 2005, pp. 935–940, doi: 10.1615/tsfp4.1550.

[43] Vreman, A. W. and Kuerten, J. G., 2014, "Comparison of direct numerical simulation databases of turbulent channel flow at $Re_\tau = 180$," Physics of Fluids, **26**(1), p. 015102.

[44] Park, N., Lee, S., Lee, J., and Choi, H., 2006, "A dynamic subgrid-scale eddy viscosity model with a global model coefficient," Physics of Fluids, **18**(12), p. 125109.

[45] Vreman, A. W., 2004, "An eddy-viscosity subgrid-scale model for turbulent shear flow: Algebraic theory and applications," Physics of Fluids, **16**(10), pp. 3670–3681.

[46] Smagorinsky, J., 1963, "General circulation experiments with the primitive equations," Monthly Weather Review, **91**(3), pp. 99–164.

[47] Iliescu, T. and Fischer, P. F., 2003, "Large eddy simulation of turbulent channel flows by the rational large eddy simulation model," Physics of Fluids, **15**(10), pp. 3036–3047.

[48] Lee, J., Kim, J., Choi, H., and Yang, K. S., 2011, "Sources of spurious force oscillations from an immersed boundary method for moving-body problems," Journal of Computational Physics, **230**(7), pp. 2677–2695.

[49] De Villiers, E., 2006, "The Potential of Large Eddy Simulation for the Modeling of Wall Bounded Flows," PhD thesis, Imperial College London.

[50] Brochu, E., Cora, V. M., and de Freitas, N., 2010, "A Tutorial on Bayesian Optimization of Expensive Cost Functions, with Application to Active User Modeling and Hierarchical Reinforcement Learning," arXiv:1012.2599

[51] Frazier, P. I. and Wang, J., 2016, "Bayesian Optimization for Materials Design," *Information Science for Materials Discovery and Design*, T. Lookman, F. J. Alexander, and K. Rajan, eds., Vol. 225, Springer, Cham, pp. 45–75.

[52] Chen, D., Skouras, M., Zhu, B., and Matusik, W., 2018, "Computational discovery of extremal microstructure families," Science Advances, **4**(1), p. eaao7005.

[53] Chen, W., Watts, S., Jackson, J. A., Smith, W. L., Tortorelli, D. A., and Spadaccini, C. M., 2019, "Stiff isotropic lattices beyond the Maxwell criterion," Science Advances, **5**(9), p. eaaw1937.

[54] Shaw, L. A., Sun, F., Portela, C. M., Barranco, R. I., Greer, J. R., and Hopkins, J. B., 2019, "Computationally efficient design of directionally compliant metamaterials," Nature Communications, **10**(1), p. 291.

[55] Song, J., Wang, Y., Zhou, W., Fan, R., Yu, B., Lu, Y., and Li, L., 2019, "Topology optimization-guided lattice composites and their mechanical characterizations," Composites Part B: Engineering, **160**, pp. 402–411.

[56] Snoek, J., Larochelle, H., and Adams, R. P., 2012, "Practical Bayesian Optimization of Machine Learning Algorithms," arXiv:1206.2944

[57] Chen, Y., Huang, A., Wang, Z., Antonoglou, I., Schrittwieser, J., Silver, D., and de Freitas, N., 2018, "Bayesian Optimization in AlphaGo," arXiv:1812.06855

[58] Oh, C., Gavves, E., and Welling, M., 2018, "BOCK : Bayesian Optimization with Cylindrical Kernels," arXiv:1806.01619

[59] Pyzer-Knapp, E. O., 2018, "Bayesian optimization for accelerated drug discovery," IBM Journal of Research and Development, **62**(6), pp. 2:1–2:7.

[60] Korovina, K., Xu, S., Kandasamy, K., Neiswanger, W., Poczos, B., Schneider, J., and Xing, E. P., 2019, "ChemBO: Bayesian Optimization of Small Organic Molecules with Synthesizable Recommendations," arXiv:1908.01425

[61] Sheikh, H. M., Shabbir, Z., Ahmed, H., Waseem, M. H., and Sheikh, M. Z., 2017, "Computational fluid dynamics analysis of a modified Savonius rotor and optimization using response surface methodology," Wind Engineering, **41**(5), pp. 285–296.

[62] Tušar, T., Brockhoff, D., and Hansen, N., 2019, "Mixed-integer benchmark problems for single- and bi-objective optimization," *Proceedings of the Genetic and Evolutionary Computation Conference*, ACM, Prague, Czech Republic, 13-17 July 2019, pp. 718–726, doi: 10.1145/3321707.3321868.

[63] Bechert, D. W. and Bartenwerfer, M., 1989, "The viscous flow on surfaces with longitudinal ribs," Journal of Fluid Mechanics, **206**, pp. 105–129.

[64] Jeong, J. and Hussain, F., 1995, "On the identification of a vortex," Journal of Fluid Mechanics, **285**, pp. 69–94.

[65] Lee, S.-J. and Lee, S.-H., 2001, "Flow field analysis of a turbulent boundary layer over a riblet surface," Experiments in Fluids, **30**(2), pp. 153–166.

[66] Bacher, E. and Smith, C., 1985, "A combined visualization-anemometry study of the turbulent drag reducing mechanisms of triangular micro-groove surface modifications," *Shear Flow Control Conference*, American Institute of Aeronautics and Astronautics, Boulder, Colorado, USA, 12-14 March 1985, doi: 10.2514/6.1985-548.

[67] Savill, A. M., 1990, "Drag Reduction by Passive Devices - a Review of some Recent Developments," *Structure of Turbulence and Drag Reduction*, A. Gyr, ed., Springer Berlin Heidelberg, Berlin, Heidelberg, Chap. 5, pp. 429–465.

[68] Choi, K.-S., 1990, "Drag Reduction Mechanisms and Near-wall Turbulence Structure with Riblets," *Structure of Turbulence and Drag Reduction*, Springer Berlin Heidelberg, Berlin, Heidelberg, Chap. 5, pp. 553–560.

[69] San Diego Supercomputer Center (SDSC), 2023, "Expanse User Guide," Accessed 2023-08-04, https://www.sdsc.edu/support/user_guides/expanse

List of Figures

List of Tables